


Summer 2018

# Laser-Induced Recoverable Surface Patterning on Ni50Ti50 Shape Memory Alloys

Saidjafarzoda Ilhom

Western Kentucky University, saidjafarzoda.ilhom056@topper.wku.edu

Follow this and additional works at: <https://digitalcommons.wku.edu/theses>

 Part of the [Condensed Matter Physics Commons](#), [Engineering Physics Commons](#), [Optics Commons](#), and the [Plasma and Beam Physics Commons](#)

---

## Recommended Citation

Ilhom, Saidjafarzoda, "Laser-Induced Recoverable Surface Patterning on Ni50Ti50 Shape Memory Alloys" (2018). *Masters Theses & Specialist Projects*. Paper 3052.  
<https://digitalcommons.wku.edu/theses/3052>

This Thesis is brought to you for free and open access by TopSCHOLAR®. It has been accepted for inclusion in Masters Theses & Specialist Projects by an authorized administrator of TopSCHOLAR®. For more information, please contact [topscholar@wku.edu](mailto:topscholar@wku.edu).

LASER-INDUCED RECOVERABLE SURFACE PATTERNING ON Ni<sub>50</sub>Ti<sub>50</sub> SHAPE  
MEMORY ALLOYS

A Thesis  
Presented to  
The Department of Physics and Astronomy  
Western Kentucky University  
Bowling Green, Kentucky

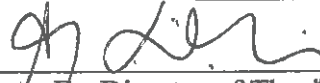
In Partial Fulfillment  
Of the Requirements for the Degree  
Master of Science

By  
Saidjafarzoda Ilhom

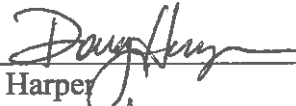
August 2018

LASER-INDUCED RECOVERABLE SURFACE PATTERNING ON Ni<sub>50</sub>Ti<sub>50</sub> SHAPE  
MEMORY ALLOYS

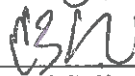
Date Recommended 06.20, 2018



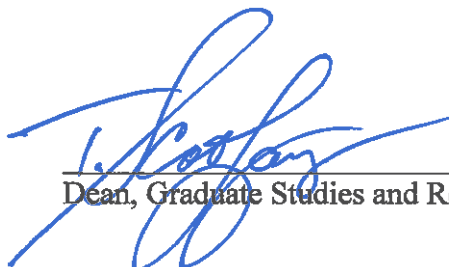
Ali Ogluz Er, Director of Thesis



Doug Harper



Muhammad Sajjad



6/25/18  
Date

Dean, Graduate Studies and Research

I would like to dedicate this thesis to my parents who have always given me the support and courage to reach for the stars and chase my dreams.

## ACKNOWLEDGMENTS

Firstly, I would like to express my sincere gratitude to my advisor Dr. Ali Oguz Er for the continuous support of my master study and research, for his patience, motivation, and immense knowledge. His supervision helped me in all the time of research and writing of this thesis. I am also so grateful to Dr. Harper and Dr. Sajjad for taking their valuable time to serve on my thesis committee. Also, I sincerely appreciate my fellow labmates dedicating their time helping me during the experiments. Finally, I would like to acknowledge the financial support of NASA, Kentucky EPSCoR, and Kentucky Science and Engineering Foundation (KSEF) without which this work would not have been possible.

## CONTENTS

ABSTRACT	vi
Chapter 1. INTRODUCTION.....	1
1.1. Shape memory alloys (SMAs).....	1
1.2. Laser-assisted surface patterning.....	3
1.3. Laser matter interaction.....	4
1.4. Surface patterning on shape memory alloys (SMAs).....	8
Chapter 2. Materials and Methods.....	11
2.1 Materials.....	11
2.2 Laser-direct scribing.....	12
2.3 Laser-assisted imprinting with preselected templates.....	13
Chapter 3. Results and Discussion.....	15
3.1. Laser direct-scribing.....	15
i. Characterization of direct-scribed NiTi shape memory alloy.....	15
ii. Eulerian model for the laser absorption on NiTi.....	20
3.2. Laser-assisted imprinting with preselected templates.....	24
i. Laser-assisted imprinting of aluminum and gold thin foils.....	24
ii. Laser-assisted imprinting of NiTi shape memory alloys.....	26
iii. Simulation of laser absorption on Copper surface.....	29
CONCLUSION.....	31
APPENDIX A: Sample preparation.....	33
APPENDIX B: ND:YAG laser operation.....	43
Literature cited.....	49

# LASER-INDUCED RECOVERABLE SURFACE PATTERNING ON Ni<sub>50</sub>Ti<sub>50</sub> SHAPE MEMORY ALLOYS

Saidjafarzoda Ilhom

August 2018

54 Pages

Directed by: Ali Oguz Er, Doug Harper, and Muhammad Sajjad

Department of Physics and Astronomy

Western Kentucky University

Shape memory alloys (SMAs) are a unique class of smart materials exhibiting extraordinary properties with a wide range of applications in engineering, biomedical, and aerospace technologies. In this study, an advanced, efficient, low-cost, and highly scalable laser-assisted imprinting method with low environmental impact to create thermally controllable surface patterns is reported. Two different imprinting methods were carried out mainly on Ni<sub>50</sub>Ti<sub>50</sub> (at. %) SMAs by using a nanosecond pulsed Nd:YAG laser operating at 1064 nm wavelength and 10 Hz frequency. First, laser pulses at selected fluences were directly focused on the NiTi surface, which generated pressure pulses of up to a few gigapascal (GPa), and thus created micro-indentations. Second, a suitable transparent overlay serving as a confining medium, a sacrificial layer, and a mesh grid was placed on the NiTi sample, whereafter the laser was focused through the confinement medium, ablating the sacrificial layer to create plasma and pressure, and thus pushing and transferring the grid pattern onto the sample. Scanning electron microscope (SEM) and laser profiler images show that surface patterns with tailorable sizes and high fidelity could be obtained. The depth of the patterns was shown to increase and later level off with the increase in laser power and irradiation time. Upon heating, the depth profile of the imprinted SMA surfaces changed where the maximum depth recovery ratio of 30 % was observed. Recovery ratio decreased and saturated at about 15 % when the number of pulses were increased. A numerical simulation of the laser irradiation process was

performed showing that considerably high pressure and temperature could be generated depending on the laser fluence. The stress wave closely followed the rise time of the laser pulse to its peak value and followed by the rapid attenuation and dispersion of the stress through the sample.



# CHAPTER 1

## INTRODUCTION

### 1.1. Shape memory alloys

In the current era of technological revolution, the development of smart, adaptive, and multi-functional systems is of great importance. However, the increased need for actuators and sensors in these systems results in undesirable outcomes such as increase in weight and volume of the corresponding system components [1]. Particularly, in the automotive and aerospace sectors where the increase in weight leads to higher fuel consumption, it is crucial to come up with novel ideas that overcome the above-mentioned downsides.

Shape memory alloys (SMAs), a unique class of smart materials that have the ability to return to their previous shapes with temperature or magnetic field, are playing a growing role in the development of mini-actuators and micro-electromechanical systems (MEMS) [1-6], automotive [7-9], aerospace [10-13] and biomedical [14-18] industries. The first discovery of the shape memory alloy dates back to 1932 by Arne Olander; however, it only became more attractive to research community in 1962 when William Buehler and Frederick Wang of Naval Ordnance Laboratory found out the shape memory effect (SME) in a Ni-Ti alloy, generally called ‘nitinol’ (combination of Ni-Ti and Naval Ordnance Laboratory) [19, 20]. Furthermore, other low-cost and commercially available SMAs are Fe-Mn-Si, Cu-Zn-Al, Cu-Al-Ni, Ni-Ti-Hf, Ni-Ti-Pd, Ni-Mn-Ga, and so forth. Among these, iron-based and copper-based SMAs are not widely utilized in industry due to their instability, brittleness, and poor thermo-mechanical performance [21, 22]. Whereas, most practical applications prefer NiTi-based SMAs due to their remarkable

corrosion resistance, biological compatibility, superelasticity, superior ductility, and large transformation strain (10%) making them suitable for biomedical devices, actuators, sensors, dampers, sealing elements, couplers, and electrical components [23, 24].

The mechanism behind the shape memory effect in such materials mainly resides in a direct solid-to-solid phase change between the higher temperature phase, austenite and the lower temperature phases twinned and de-twinned martensite upon applying a stress or temperature as illustrated in Figure 1.1, or a magnetic field in the case of magnetic shape memory alloys. Basically, at lower temperatures SMAs are in the twinned

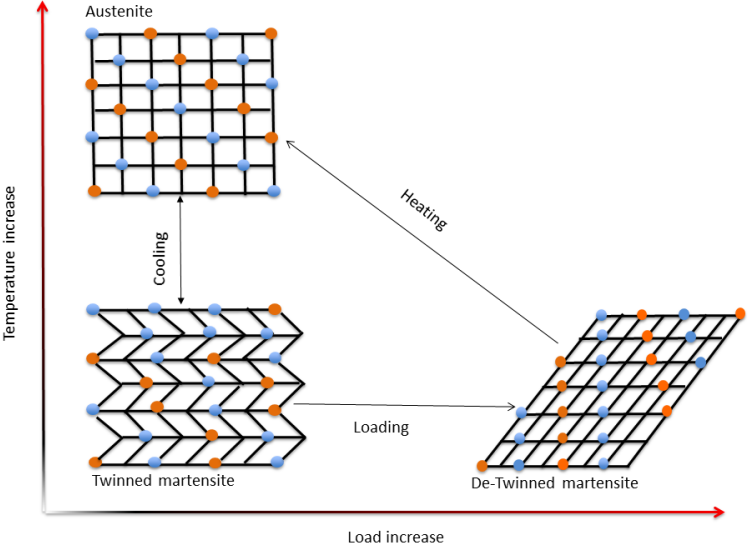


Figure 1.1. Schematic showing the shape memory effect due to phase transformations.

martensite phase, a monoclinic crystal structure with multiple possible martensite variants. When a stress is applied, these highly displacive domains reorient into the de-twinned phase, also called stress-induced martensite transformation, which results in large macroscopic inelastic strain, and thus retained shape change. Once the sample is heated to a certain temperature the stress-induced martensite variants thermoelectrically

rearrange to the higher temperature austenite phase, generally a cubic crystal structure leading to the shape recovery. Next, when the material cools down in the absence of an external stress, the martensite domains reorganize themselves back to the martensite phase in a self-accommodating way via twinning, which compensates for the elastic strains generated around the martensite variants, and thus resulting in no further observable macro-structural shape changes [25-28].

## 1.2. Laser-assisted surface patterning

Micro/nanoscale patterning onto metallic components has gained great importance in aerospace, microelectronics, and biomedical sectors [29-32]. Currently, existing lithography-related routes, such as nanoimprint [33-35] and step and flash imprint [36, 37] have been extensively employed to achieve sub-micron/nanoimprints, but are limited to only polymeric materials. Moreover, these methods suffer from several drawbacks such as high cost, complex procedures, low reproducibility and throughput, and adverse environmental effects [38, 39]. Alternatively, lasers have opened new means to fabricate such periodic structures not only on polymers but also on ceramics and metals in a wide range of industries [39-42]. Surface patterning by lasers is flexible, environmentally friendly, remote and contact-free, precise, scalable, and does not involve any heating or etching processes [39, 43]. Examples of laser patterning techniques include laser shock peening and laser direct-write (also known as laser scribing), and laser shock forming [44-50]. In laser shock peening a high energy laser beam is directed onto an ablative layer placed between material and dielectric medium, which serves as a tamping medium for the laser generated shock wave [51]. Consequently, the shock wave leads to a high compressive residual stress due to severe plastic deformation, which has been reported to

significantly increase the fatigue life of materials used in a broad range of industrial applications [52-56]. Similarly, in laser-assisted direct-write, a high power laser pulse directly interacts with materials in a thin layer of material [47, 57]. Consequently, laser pulses induce high amplitude plasma pressure ( $>1$  GPa) in a short duration (usually on the order of  $10^{-9}$  seconds) that creates a strong shock wave, and form three-dimensional structures [26].

### 1.3. Laser matter interaction

Understanding the underlying physical phenomena taking place during laser interaction with the matter is worth considering to better grasp the mechanisms of laser-assisted material processing so as to develop the most accurate tools and techniques for particular application requirements. The mechanism of laser interaction with materials is rather a complex physical phenomenon that involves several processes, such as photothermal, photochemical, hydrodynamical, and ultrafast laser interaction depending on the length of the laser pulse [58-60]. Photothermal process occurs when the pulse width is longer (on the order of nanoseconds) than the electron-phonon relaxation time and the electron heat conduction time, the time after which the electrons and lattice are at thermal equilibrium. During this process the laser is mainly absorbed by the free electrons via inverse Bremsstrahlung interaction heating up the lattice, and thus melting and vaporizing the target as well as resulting in various undesired consequences such as large heat affected zones, severe melting of laser processed areas, surface debris, surface ripples due to shock-stresses, and micro-cracks, Figure 1.2(a) [58]. Conversely, ultrafast laser interactions happen when the laser pulse width is shorter than the electron-phonon energy relaxation time, where the interaction is considered as non-thermal and involves various

physical phenomena, such as electronic excitation and ionization, non-thermal melting, and electron-lattice heating [29, 61]. In particular, in the material processing using femtosecond pulses where the pulse width is on the orders of  $10^{-15}$  seconds, significantly smaller than the electron-phonon coupling time ( $\sim 10^{-12}$  seconds), the process is completely non-thermal that offers a wide range of unique advantages over the conventional thermal laser processing that typically employs nanosecond and longer pulses [29, 62, 63]. Due to better spatial concentration of ultrashort pulses compared to nanosecond ones, they decrease the required laser power for ablation, increase the thermal gradient in the target, and increase the energy coupling to initiate direct solid-to-vapor transition, and thus suppress thermal diffusion and prevent undesired heat affected zones and surface debris

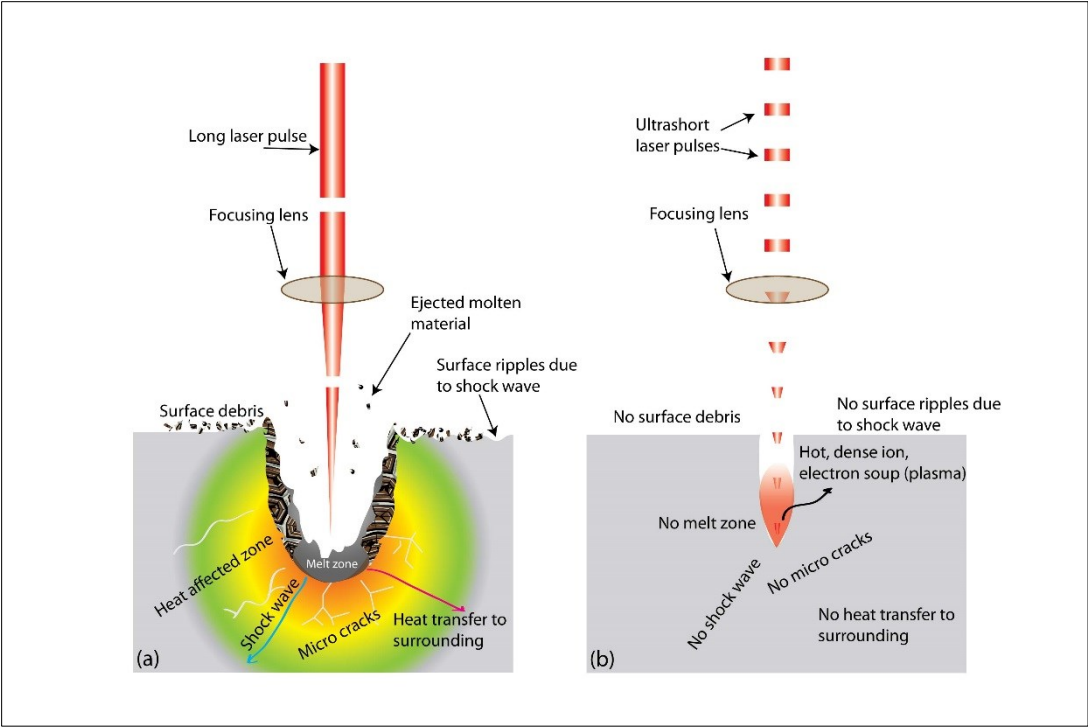


Figure 1.2. (a) Effects of material processing using longer and (b) ultrashort laser.

formations, Figure 1.2(b) [29]. However, depending on the purpose and type of specific applications, each of these processing routes has their own advantages and disadvantages.

For instance, for the applications where residual heat and stress is necessary in modifying the microstructural properties of materials during laser treating, photothermal laser processing becomes handier; while, ultrafast laser techniques come into play in applications where the laser processing requires extremely high precision and accuracy. Photochemical process, yet another laser matter interaction mechanism, takes place when the laser energy is directly absorbed by the chemical bonds leading to bond fragmentation, but this mechanism generally requires sufficiently high laser photon energy to be able to photochemically break the bonds [64]. Finally, hydrodynamical process takes place when transient melting occurs on the surface leading to bulk material, droplet, and particulates being formed and expelled from the target [26].

In the subsequent laser processing stages, the ablated material forms a plasma plume as follows. The mean free path of visible and near infrared laser radiation in metals is on the order of a few nanometers, so the laser pulse of sufficient energy is initially absorbed predominantly by a very thin layer of material. Due to rapid energy deposition

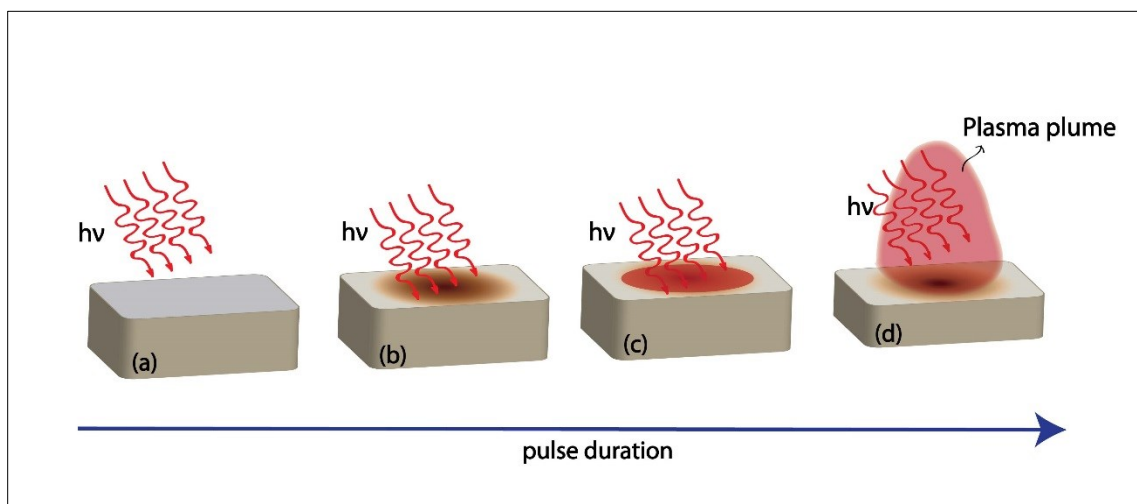


Figure 1.3. Plasma plume formation during laser interaction with the material.

time, thermal diffusion of energy is only limited to at most a few nanometers in the interaction zone, which leads to a sharp temperature gradient in penetration depth heating and vaporizing the material, Figure 1.3(b)-(c). Consequently, the vaporized material is ionized by the subsequent laser pulses and transformed into a plasma plume, Figure 1.3(d) [47, 57]. This plasma is highly luminous, forward-directed, and transient in nature. The properties of laser-produced plasma, such as degree of ionization and temperature of plasma species, can evolve quickly and strongly and depend on various parameters such as the laser wavelength, energy density, repetition rate, pulse duration, spot size on target, target composition, and surface quality [65, 66]. The as-generated plasma continues to strongly absorb the laser energy where the temperature of the plasma rises extremely rapidly, on the orders of  $10^{11}$  Kelvin/second, which is thought to occur due to inverse-Bremsstrahlung absorption of the laser radiation. The principle of inverse-Bremsstrahlung absorption is that when enough photon energy is incident through a volume of atoms, it excites the atoms within that volume to the extent that they are stripped of their electrons and become ionized, and thus form plasma [26, 58, 67]. Since the material experiences a phase transformation from solid to vapor, a pressure (shock) wave is generated that propagates through the depth of the sample, Figure 1.4(a) [57]. An analogy to better visualize this process can be thought of as the plasma being the fuel combustion from the rocket exhaust and the shock-wave being the generated thrust that propels the rocket. Next, the energy is redistributed between the energy of plume and shock waves during expansion which is usually around 100 ns [58, 67]. Furthermore, when an additional transparent overlay is used, enhanced pressures (4-10 times higher) on the material surface could be achieved and gas breakdown loss be prevented, Figure 1.4(b) [43, 47]. When the

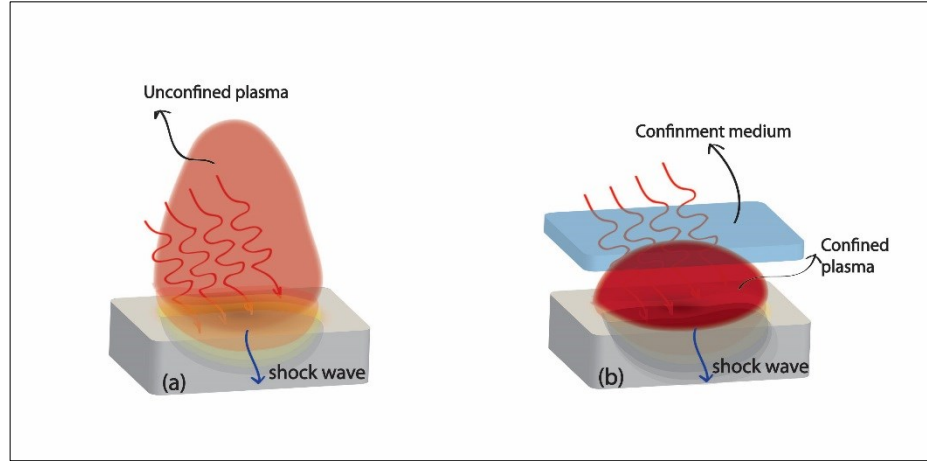


Figure 1.4. Shock wave generation due to (a) unconfined (b) confined plasma.

magnitude of the primary shock-wave front of the laser exceeds the dynamic yield strength of the material, termed as the Hugoniot Elastic Limit (HEL), it plastically deforms the microstructure and creates added dislocations in the material until the shock-wave attenuates below HEL [68]. It should be noted that while SMAs don't appear to exhibit a HEL like other metals, the amount of deformation depends on the pressure [69]. Therefore, it is important to estimate the peak pressure which can be found by [68]

$$P \text{ (GPa)} = 0.01 \left[ \frac{Z \text{ (gcm}^{-2}\text{s}^{-1}) I_0 \text{ (GW/cm}^2\text{)} \delta}{2\delta + 3} \right]^{1/2}$$

where  $I_0$  is the incident laser power density,  $P$  is the pressure, and  $Z$  is the reduced acoustic impedance between a target and medium, and  $\delta$  is the efficiency of plasma material interaction.

#### 1.4. Surface patterning on shape memory alloys (SMAs)

Recently, morphing at micro and macro scales on shape memory alloys has attracted considerable interest [11]. Indentation-induced shape memory effect and superelasticity on such compounds have been previously observed under complex loading conditions [70-72]. Specifically, shallow spherical indents in austenite NiTi specimen



were shown to fully recover upon unloading, but indents in martensite could only partially recover upon unloading while additional recovery occurred upon heating to the austenite phase [73]. Moreover, experimental indentation testing under spherical indenter revealed a “self-healing” effect and reversible protrusions upon thermal cycling [30, 74]. Thermal cycling on SMAs which may be repeated indefinitely, results in a ‘bumpy’ and a flat surface, where the geometry of the protrusion primarily depends on the processing parameters and material properties [75, 76]. As an alternative, laser-assisted surface patterning on SMAs will also generate such controllable surfaces in a remote and contactless way, with much precise modification of the surface by rather having more accurate energy deposition than conventional indentation techniques. In addition, shape memory alloys can produce very high actuation strain (8% uniaxial strain), stress (~400 MPa) and work output (~10 MJ/m<sup>3</sup>) as a result of reversible martensitic phase transformations [23]. Consequently, such properties together with smart controllable surface features might have favorable outcomes in the aerodynamics of moving objects since the surface roughness and texture can drastically alter the characteristics of turbulent flow, and thus the drag and friction forces exerted on the surface of the moving objects [77, 78]. Indeed, it has been reported that the “riblets” on the shark skin can reduce the wall shearing stress or wall friction up to 10% while many other surface structures are known to increase friction and drag force [79, 80]. For micro-morphing, shape memory surfaces can be produced by embedding patterned SMAs into aircraft structure and forming “hybrid structures” [81, 82]. The temperature change (e.g. triggered by electrical current) will activate SMAs and the surface geometry will change upon phase transformation where transformed surfaces could generate very different drag or friction

forces that can be optimized for aircraft operation.

A recent study has shown that patterned microindents can be generated on the surface of NiTi SMA by laser-assisted imprinting in a relatively easier and faster way rather than etching-related patterning techniques when the laser beam is focused on preselected pattern on the target material [39]. Although laser-assisted imprinting (mask is used between material and dielectric media in this technique) was shown to be promising in creating active surfaces [39], the effects of laser parameters as well as material properties on the indent geometry and shape recovery properties have not been investigated in detail. In this study, we have employed two relatively different routes to create micro-patterns on NiTi shape memory alloys. In the first method, which we have named as the laser-direct scribing, we create micro-patterns by directly focusing the laser onto the NiTi SMA surface without placing any sacrificial layer and confinement medium in between. However, in the second technique, which we have termed as the laser-assisted imprinting with preselected templates, we have used a sacrificial layer and a confinement medium to imprint the outline of these predefined templates on the NiTi shape memory alloys. Next, we have analyzed the changes in depth of the generated patterns on NiTi SMAs with respect to the laser power density and irradiation time. We have also explored these laser parameters' effects on the indents' shape memory behavior of NiTi SMAs of laser direct-write method and reported optimum conditions to generate patterns with the highest shape recovery ratio. Numerical simulation of shock wave evolution and propagation was also performed to better understand the underlying laser-induced shock waves [83, 84].

## CHAPTER 2

### MATERIALS AND METHODS

#### 2.1. Materials

Vacuum induction melted Ni<sub>50</sub>Ti<sub>50</sub> (at. %) shape memory alloys were cut into circular plates with a diameter of 10 mm and thickness of 1 mm by electrical-discharge machining method. The surface roughness of the samples were reduced to 0.05  $\mu\text{m}$  in five steps by using Buehler EcoMet 250 Grinder-Polisher with an AutoMet 250 Power head. Transformation temperatures were determined by using a Perkin-Elmer Pyris 1 differential scanning calorimeter (DSC). The martensite and austenite start and finish temperatures ( $M_s$ ,  $M_f$ ,  $A_s$ , and  $A_f$ , respectively) are 78 °C, 45 °C, 85 °C and 122 °C for the these samples and they will be referred as 1 mm thick NiTi samples . Moreover, 25  $\mu\text{m}$  thick nitinol foil (Alfa Aesar 47169, flat annealed, pickled surface), which has an approximate austenite finish temperature of 45 °C was also obtained to examine the effects of laser-assisted patterning on thinner NiTi SMA. In addition, commercially available aluminum foil (Reynolds Wrap (Heavy Duty)) was utilized for both patterning and also as a sacrificial layer. An industrial graphite dry lubricant spray (Blaster) was also used as an ablative layer at certain parts of the experiments that will be explicitly mentioned in the text when pertinent. Pre-cleaned micro slides (Sargent-Welch) were utilized as the confinement medium. The laser in our lab that was used for all of the patterning experiments is a nanosecond Nd:YAG pulsed laser Continuum Surelite II. Laser has a fundamental wavelength of 1064 nm, pulse width of 5 nanosecond, 10 Hz repetition rate and Gaussian shape with 6 mm diameter of unfocused beam (measured at  $1/e^2$ ).

## 2.2. Laser-direct scribing

A typical experimental setup for the laser direct-scribing route of shape memory alloys can be seen in Figure 2.2.1. Direct-scribing was performed by ablating the 1 mm thick NiTi samples' surface with the focused laser beam at the repetition rate of 10 Hz with the fluences between 0.18 - 0.71 J/cm<sup>2</sup> calculated at the unfocused spot size of 6 mm from 10 to 160 pulses. Laser energy was held constant and a lens of 5 cm was used to focus the laser beam on NiTi surface translated by a motorized stage. Morphological

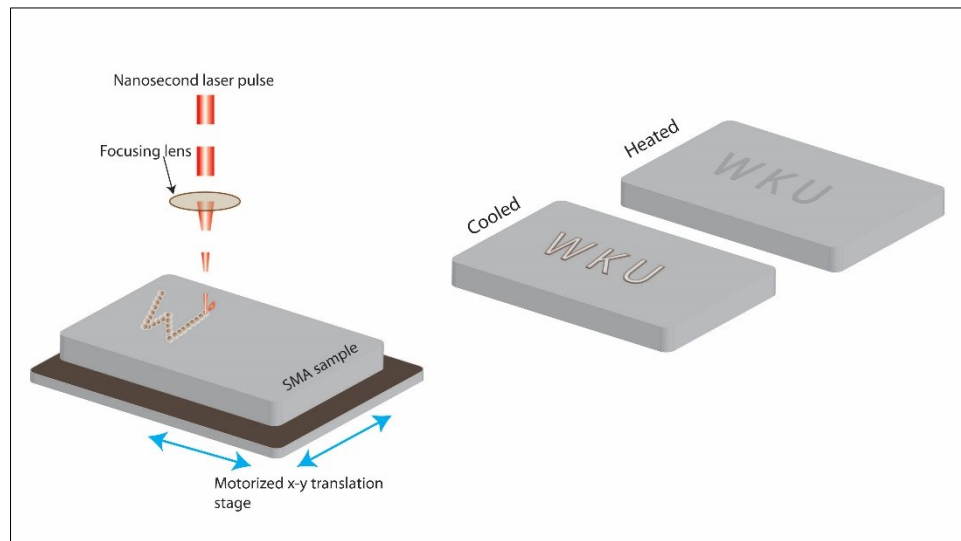


Figure 2.2.1. A typical experimental setup for laser direct scribing of SMAs.

properties were investigated by VHX-1000 Digital Microscope (Keyence) and the recovery depth measurements were analyzed by the laser profiler (Zygo, NewView 7300). In order to examine the spot size effect, an aspheric focusing lens of 5 cm and a convex lens of 20 cm (Thorlabs) were used. To observe the recovery effect of the samples, initial depths at room temperature were measured. Then, each sample was placed onto a heating stage (Marlow Industries, Inc. TG12-8L) where the temperature monitored by a pyrometer reached up to 160° C and the resulting depth changes were compared.

### 2.3. Laser-assisted imprinting with preselected templates

Laser imprinting using mesh grid templates as a mask was carried out in two different ways. First, a thin graphite layer of approximately 15  $\mu\text{m}$  was sprayed on the 1 mm thick NiTi sample to increase the pressure and to protect the material from damage caused by ablation and melting. Next, on top of the graphite layer, a copper grid (SPI Supplies) was used as both an ablative material and punch, and a piece of BK7 glass was used as both an ablative material and punch, and a piece of BK7 glass was used to confine the plasma generated by the nanosecond laser, Figure 2.3.1(a). Hereafter,

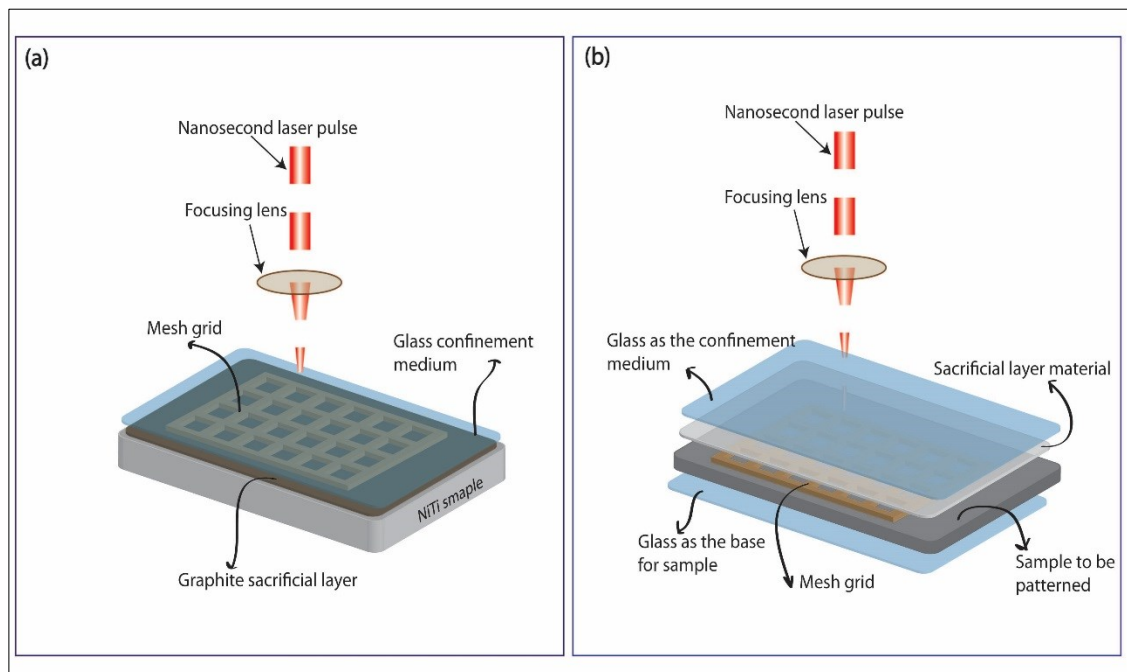


Figure 2.3.1 Experimental setups for the laser-assisted imprinting using predefined mesh templates.

this method will be referred as ‘method M1’ throughout the text. In the second route, which is specifically more convenient for the patterning of thinner (a couple of micron thick) samples, the sample is initially placed on a glass, then the mesh grid is laid onto the sample. But, at this time a thin aluminum foil (Reynolds) is used as an ablative layer on top of mesh grid, which is then covered by another piece of glass serving as a confinement

medium, Figure 2.3.1(b). This second method will be referred as ‘method M2’ hereafter. Next, samples prepared were irradiated by selected laser fluences with the focused beam diameter of 3 mm. The expansion of plasma created on the ablative layer is confined by confinement medium, mainly glass, pushes the grid onto the surface. This highly dynamic force creates plastic deformation on the surface leading a surface pattern which is similar to the hole of the copper grid. After the irradiation, copper grid was peeled off and the graphite layer was washed off by acetone for the samples patterned via the first method, ‘method M1’. However, there was no need of washing the samples patterned via the second route of ‘method M2’, since the ablation mainly takes place on the first aluminum sacrificial layer leaving the surface of the patterned sample undamaged and clean. Morphological properties of the surface were investigated by SEM (Jeol 6510LV) and the light microscope (Keyence VHX500F). Laser parameters were adjusted to optimize the protrusion heights.

## CHAPTER 3

### RESULTS AND DISCUSSIONS

#### 3.1. Laser direct-scribing

##### i. Laser direct-scribing and characterization of NiTi shape memory alloys

In general, laser processing parameters include substrate temperature, background gas pressure, laser wavelength, pulse width, repetition rate, and fluence. Among these, laser fluence is an important parameter to obtain effective material removal and stress creation on a surface since different mechanisms come in to play depending on the value of the fluence. For instance, laser heating with fluence below the ablation threshold can lead to many temperature dependent processes such as reorganizing the crystal structure, enhancing diffusion rates, and sintering of porous material [85]. Once the fluence is above the ablation threshold, the formation of transient pools of molten material on the surface can be observed and material will be ejected [86]. In nanosecond laser ablation, ablation is considered as conventional equilibrium evaporation and thermal ablation. The laser is absorbed by the target and it heats up the lattice, which will then melt and vaporize the target. A portion of the vaporized material will then be ionized by the high incident beam via the inverse bremsstrahlung effect inside the penetration depth. The material will then form a forward directed plasma plume that moves away due to Coulomb repulsion and recoil from the target, which in turn induces a shock-wave pushing the target surface, and thus creating an indent [47, 58, 67]. By adjusting the laser fluence carefully, the microstructure and surface properties of the SMAs can be tailored. Figure 3.1.1 is the three-dimensional (3D) laser profiler image of such an indent generated with the laser fluence of  $0.35 \text{ J/cm}^2$ . Achieving a high laser ablation efficiency is of paramount

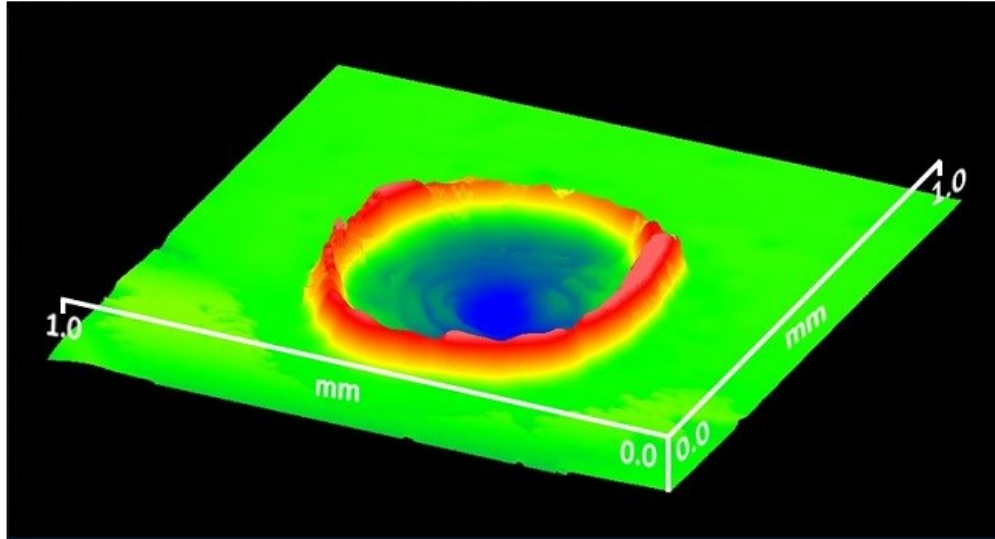


Figure 3.1.1. 3D plot of the as-created indent at  $0.35 \text{ J/cm}^2$  by the laser direct-scribing of NiTi SMAs.

importance to achieve a reasonable amount of material removal and stress creation on the sample. Normally, the laser energy density slightly higher than the ablation threshold results in efficient material removal and ablation depth. If applied laser energy density is below the threshold, no material will be removed. Conversely, in the case of applying an excess amount of energy, only the energy required for material removal will be used while the remaining energy will be dissipated as a heat. This excess heat will cause unwanted debris, cracking, melting, and stress in the surrounding material. This phenomena, also known as heat affected zone (HAZ), is one of the disadvantages of the laser material removal and it mainly depends on the laser pulse duration and wavelength [87]. In fact, the recast layer profiled in red color around the indent in Figure 3.1.1 is one of the consequences of HAZ. Nonetheless, the nanosecond laser pulses separated by several tens of nanosecond have been shown to improve material removal rate up to 10 times and create less HAZs compared to microsecond and longer laser pulses [88]. Alternatively, patterning with lasers having smaller pulse width, such as picosecond and femtosecond



generally result in no HAZs at all because of their non-thermal ablative nature. However, this might not be practical for creating recoverable patterns on SMAs. Since the residual heat that might have crucial effect on the shape recovery effect of the as-created patterns, lacks in the ultrashort laser imprinting, and thus may result in lower recovery rates, which still needs further investigation.

In order to study the effects of the laser fluence on the recovery of the patterned SMAs, first laser profilometer depth measurements were recorded. Figure 3.1.2 shows the maximum depth of patterns after laser imprinting with fluences ranging from 0.18 J/cm<sup>2</sup> to 0.71 J/cm<sup>2</sup> from 10 to 160 pulses. A laser fluence of 0.18 J/cm<sup>2</sup> produced a depth of ~10 μm after 10 pulses of irradiation and ~50 μm after 80 pulses. In general, the depth increased with increase in energy and duration. At 10 pulses irradiation, the depth

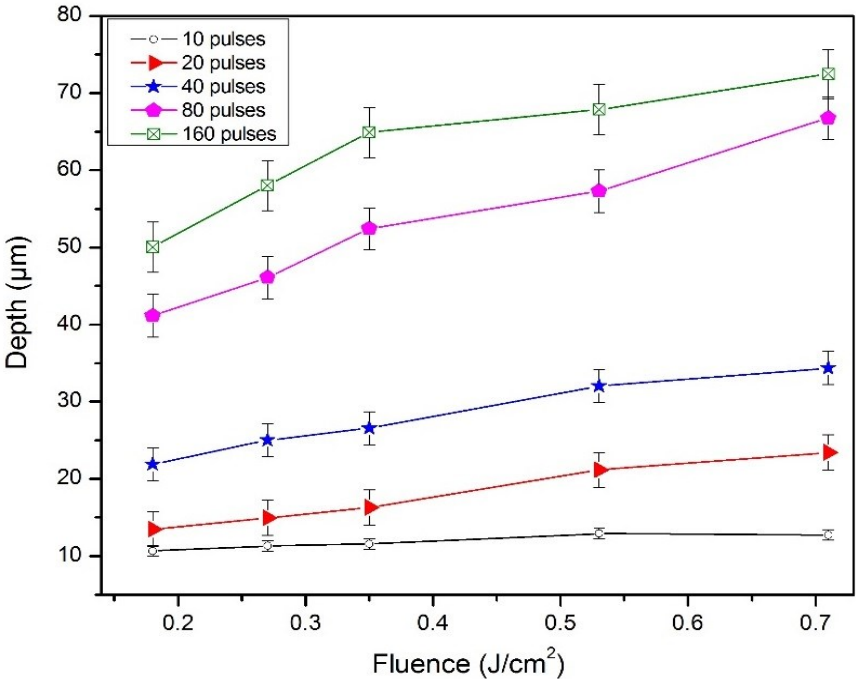


Figure 3.1.2. Depth of indents as a function of laser fluence and number of pulses.

increased slightly with increasing laser power. Increasing the laser fluence increases the kinetic energy of the particles being ejected from the target where the maximum depth of

around 70  $\mu\text{m}$  was obtained with 0.71  $\text{J}/\text{cm}^2$  and 160 pulses. The laser energy transmission in target material is mainly governed by Beer-Lambert's law and above the ablation threshold, thickness or volume of material removed per pulse typically shows a logarithmic increase with fluence according to this law given by [86]:

$$I = I_0 \exp(-\alpha z)$$

where  $I$  is laser intensity at a distance  $z$  from surface,  $I_0$  is the laser intensity at the top surface, and  $\alpha$  is the absorption coefficient that is wavelength dependent. Indeed, the increase trend in depth of scribed indents, as illustrated in Figure 3.1.2, follows the Beer-Lambert's law, initially sharp increase and later level off, which would be more evident if the data for lower laser fluences was also considered.

In order to determine the recovery of as-patterned SMA surfaces, samples were heated to 160  $^\circ\text{C}$  and their depth profile and maximum depths were measured, as shown in Figure 3.1.3. Linear depth profiles were measured at 4 different positions to get better reliability. Upon the determination of maximum indent depth at 160  $^\circ\text{C}$ , the recovery rate

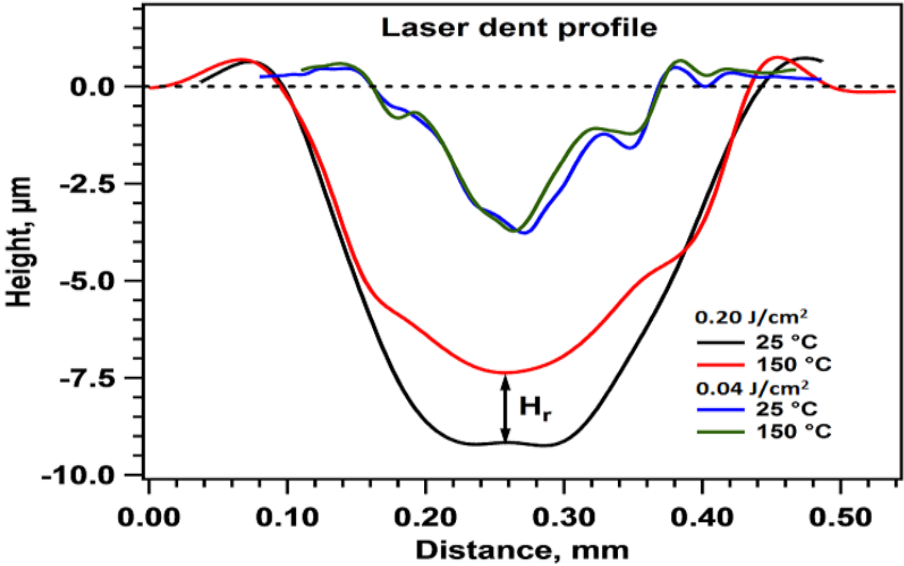


Figure 3.1.3. Shape recovery effect for indents created at two different laser fluences.

(the difference in depth between hot and cold states divided by the cold state) was calculated as a functions of laser fluence and duration, as shown in Figure 3.1.4.

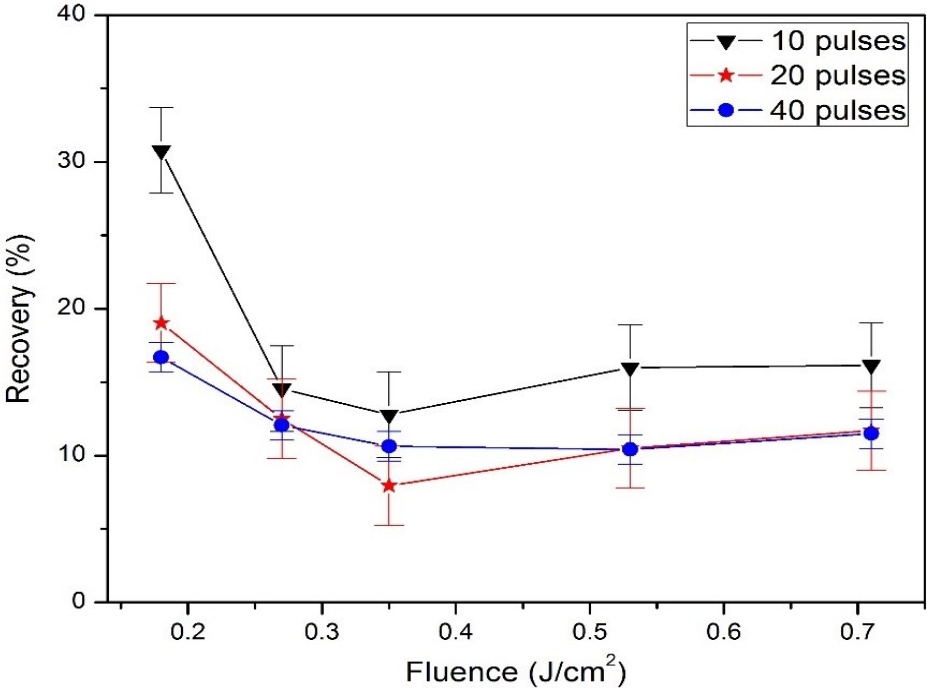


Figure 3.1.4. Recovery ratio with respect to the laser fluence and number of pulses.

Basically, at room temperature, laser direct-scribing generates stress on the sample, which results in stress-induced martensite reorientation. Upon heating, reoriented martensite transforms back to austenite, resulting in a shape change. The direction and amount of the shape change highly depends on the factors, such as type, direction, volume fraction of reoriented martensite variants, amount of plastic deformation, and direction and magnitude of internal stress [89, 90]. Thus, the depth recovery of the patterns is observed due to the transformation of reoriented martensite variants to austenite upon heating. The amount of laser fluence, one of the critical parameters to influence the abovementioned factors, has to be optimized to get the best recovery rate, since an applied stress above a certain level may cause a decrease or even not produce any shape memory

effect [69, 91], as shown in Figure 3.1.3 for the laser fluence of  $0.04 \text{ J/cm}^2$ . A recovery of more than 30% was obtained when the laser fluence was  $0.18 \text{ J/cm}^2$  and irradiation time was 1 second with total 10 pulses. The recovery ratio decreased to 20% when the sample was irradiated for two seconds (20 pulses). Further decrease in the recovery was observed for 4 seconds (40 pulses). In general, recovery decreased with time, which could be attributed to the surface damage caused by preceding pulses. When laser fluence is increased to  $0.27 \text{ J/cm}^2$ , average recovery decreased substantially. Laser energy density above  $0.27 \text{ J/cm}^2$  resulted in constant recovery of about 15%. It is not fully clear of why the recovery ratio decrease at  $0.27 \text{ J/cm}^2$  but it might be attributed to the amount of created pressure that will affect the plastic deformation. It should be noted that shape memory properties are highly internal stress and plastic deformation dependent [89, 90]. Moreover, the amount of plastic deformation and internal stresses depend on the size and temperature profile of the affected zone of imprinting process. The annihilation of plastic strain and internal stresses will increase with the exposure of the material to higher temperatures and longer times that might have led to decreased shape recovery.

ii. Eulerian model for the laser absorption on NiTi

It is well known that lasers can produce high temperature and high pressure when absorbed by a material. In most of the practical applications, it is critical to determine the heat transfer mechanism for accuracy of laser processing. To better understand the pressure propagation inside shape memory alloys, a numerical simulation of pressure evolution in shape memory alloys irradiated by a focused nanosecond pulsed laser was conducted using the fifth-order weighted essentially non-oscillatory finite volume method [92, 93] coupled with a Mie-Gruneisen model [94].

In the Eulerian setting, the governing equations in two dimensions can be written as a system of conservation laws [94]

$$\frac{\partial U}{\partial t} + \frac{\partial F}{\partial x} + \frac{\partial G}{\partial y} = S$$

where the vector of conserved quantities  $U$ , convective fluxes  $F$  and  $G$ , as well as the source term  $S$  are

$$U = \begin{bmatrix} \rho \\ \rho u \\ \rho v \\ E \\ s_{xx} \\ s_{yy} \\ s_{xy} \end{bmatrix}, F = \begin{bmatrix} \rho u \\ \rho u^2 + P - s_{xx} \\ \rho uv - s_{xy} \\ u(E + P) - us_{xx} - vs_{xy} \\ us_{xx} \\ us_{yy} \\ us_{xy} \end{bmatrix}, G = \begin{bmatrix} \rho v \\ \rho uv - s_{xy} \\ \rho v^2 + P - s_{yy} \\ v(E + P) - vs_{yy} - us_{xy} \\ vs_{xx} \\ vs_{yy} \\ vs_{xy} \end{bmatrix}, S = \begin{bmatrix} 0 \\ 0 \\ 0 \\ Q \\ \varphi_{xx} \\ \varphi_{yy} \\ \varphi_{xy} \end{bmatrix}$$

In the above equations,  $E = \rho(e + (u^2 + v^2)/2)$  is the total energy per unit volume where  $e$  is the internal energy per unit mass,  $\rho$  is the material density,  $u$  and  $v$  are the velocity components,  $s_{xx}$ ,  $s_{yy}$ ,  $s_{xy}$  are the deviatoric stresses, and  $P$  is the pressure which is obtained from Mie-Gruneisen equation of state model [94]

$$P = P_0 + \frac{c_0^2 \rho_0 \rho (\rho - \rho_0)}{[\rho - s_0 (\rho - \rho_0)]^2} + \Gamma_0 \rho_0 \left[ e - e_0 - \frac{1}{2} \left( \frac{c_0 (\rho - \rho_0)}{\rho - s_0 (\rho - \rho_0)} \right)^2 \right]$$

where  $s_0$  and  $\Gamma_0$  are Gruneisen constants and  $P_0$ ,  $\rho_0$ ,  $e_0$  and  $c_0$  are initial pressure, density, internal energy and sound velocity, respectively. The bulk speed of velocity can be computed by

$$c_0 = \sqrt{u_l^2 - \frac{4}{3} u_s^2}$$

where  $u_l$  is the longitudinal speed of sound and  $u_s$  is the shear speed of sound for the material. The parameters in the source term are

$$\varphi_{xx} = s_{xx}\Sigma + 2\Omega s_{xy} + 2G_0 \left( \frac{\partial u}{\partial x} - \frac{1}{3}\Sigma \right)$$

$$\varphi_{yy} = s_{yy}\Sigma - 2\Omega s_{xy} + 2G_0 \left( \frac{\partial v}{\partial y} - \frac{1}{3}\Sigma \right)$$

$$\varphi_{xy} = s_{xy}\Sigma + 2\Omega(s_{yy} - s_{xx}) + G_0 \left( \frac{\partial u}{\partial y} + \frac{\partial v}{\partial x} \right)$$

where  $G_0$  is shear modulus. The dilatation and spin terms can be written as

$$\Sigma = \frac{\partial u}{\partial x} + \frac{\partial v}{\partial y}$$

$$\Omega = \frac{1}{2} \left( \frac{\partial u}{\partial y} - \frac{\partial v}{\partial x} \right)$$

where we use standard central difference schemes to compute derivatives in these terms.

The stress terms are modified according to a simple radial return algorithm using the von Mises yield criterion. If the von Mises condition meets (i.e.,  $q \geq Y_0$ ), then the deviatoric stresses can be modified as [48, 95]

$$s_{xx} = s_{xx}Y_0/q$$

$$s_{yy} = s_{yy}Y_0/q$$

$$s_{xy} = s_{xy}Y_0/q$$

where  $Y_0$  refers to the yield stress and  $q$  is given by

$$q = \sqrt{3(s_{xx}^2 + s_{yy}^2 + s_{xy}^2 + s_{xx}s_{yy})}.$$

The material's data for NiTi are [96];  $\rho_0 = 6.42 \text{ g/cm}^3$ ,  $Y_0 = 560 \text{ MPa}$ ,  $G_0 = 83 \text{ GPa}$ ,  $u_l = 5360 \text{ m/s}$ , and  $u_s = 1800 \text{ m/s}$ . Therefore, the bulk velocity of the sound is 4940 m/s, which has been used to determine the computational time step according to the

Courant–Friedrichs–Lewy criterion. The Gruneisen parameters are  $\Gamma_0 = 1.497$  and  $s_0 = 1.249$ .

Finally, the absorption of laser energy is modeled by the volumetric heat source term for the energy equation [48, 95]

$$Q = I_0(1 - R)\alpha e^{(-\alpha(y_s - y) - \frac{(x - x_s)^2}{r_0^2} \frac{t^2}{t_0^2})}$$

where  $I_0$ ,  $R$ ,  $\alpha$ ,  $t_0$  and  $r_0$  are laser energy intensity, reflectance, absorption coefficient, pulse width and the beam radius, respectively. Here,  $(x_s, y_s)$  is the surface coordinates of the laser beam center and  $z = y_s - y$  measures the depth from the surface as usually described by Beer's law. Using the refraction and extinction coefficients for nitinol, we estimate  $R = 0.7$  and the absorption coefficient  $\alpha = 5.817 \times 10^7 \text{ m}^{-1}$ . In our simulations, the computational domain size is  $400 \text{ }\mu\text{m} \times 200 \text{ }\mu\text{m}$ , and the center of laser radius is located at  $x_s = 0$ ,  $y_s = 200 \text{ }\mu\text{m}$ . Initial condition is  $P_0 = 0.1 \text{ MPa}$  and we impose transmissive boundary conditions.

Our simulation results show that pressure is strongly dependent on the value of total incident laser energy density and the threshold value for pure heat conduction. The shock wave closely follows the laser pulse profile which is an initially sharp increase followed by exponential decay, as shown in Figure 3.2(a). This figure illustrates the surface pressure evolution computed at  $(x_s, y_s)$  for the intensity values between  $I_0 = 1.4 \times 10^{16} \text{ W/m}^2$  and  $5.6 \times 10^{16} \text{ W/m}^2$ . The hydrostatic pressure of 300 MPa could be generated when laser power of  $1.4 \times 10^{16} \text{ W/m}^2$  ( $0.18 \text{ J/cm}^2$ ) is used. The peak pressure value increased with laser energy density. Figure 3.2(b) shows the propagation of hydrostatic pressure for  $0.18 \text{ J/cm}^2$  laser energy density. It can be seen that pressure reach

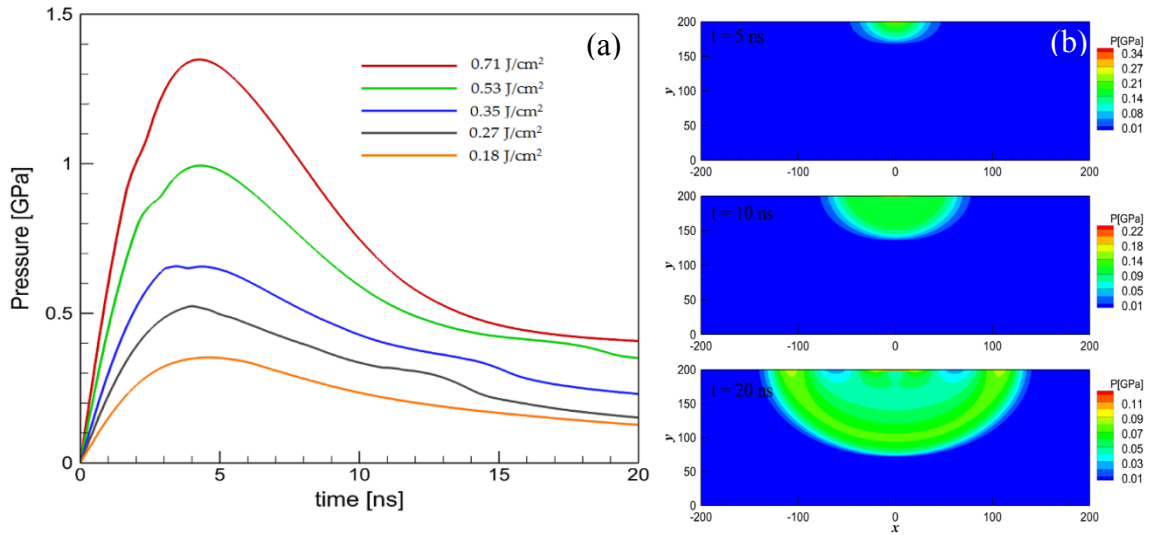


Figure 3.2. (a) Stress-wave evolution as a function of laser fluence and (b) stress-wave propagation inside NiTi for the laser fluence of  $0.18 \text{ J/cm}^2$ .

peak value at around 5 ns and it propagates through the medium with decreasing amplitude reaching almost third of its original value after 20 ns. Further simulations can also be used to determine stress/strain evolution and shock wave propagation.

### 3.2 Laser-assisted imprinting with preselected templates

#### i. Laser-assisted imprinting of aluminum and gold thin foils

As a proof of concept, initially aluminum and gold thin foils were patterned via laser-assisted imprinting with different mesh grid templates. Figure 3.2.1 shows successful imprinting of hexagonal copper grid onto aluminum sample with a single pulse at the laser fluence of  $6.4 \text{ J/cm}^2$ . Aluminum samples have smooth surface after imprinting. The hexagonal grid has 698 lines/inch, hole width of  $29 \mu\text{m}$ , pitch width of  $37 \mu\text{m}$  and bar width of  $8 \mu\text{m}$  with diameter of 3 mm. After irradiation, patterned surface is visible with optical microscope and scanning electron microscope (SEM). These patterns were generated under the outlined area of copper grid which shows the ablation of the copper



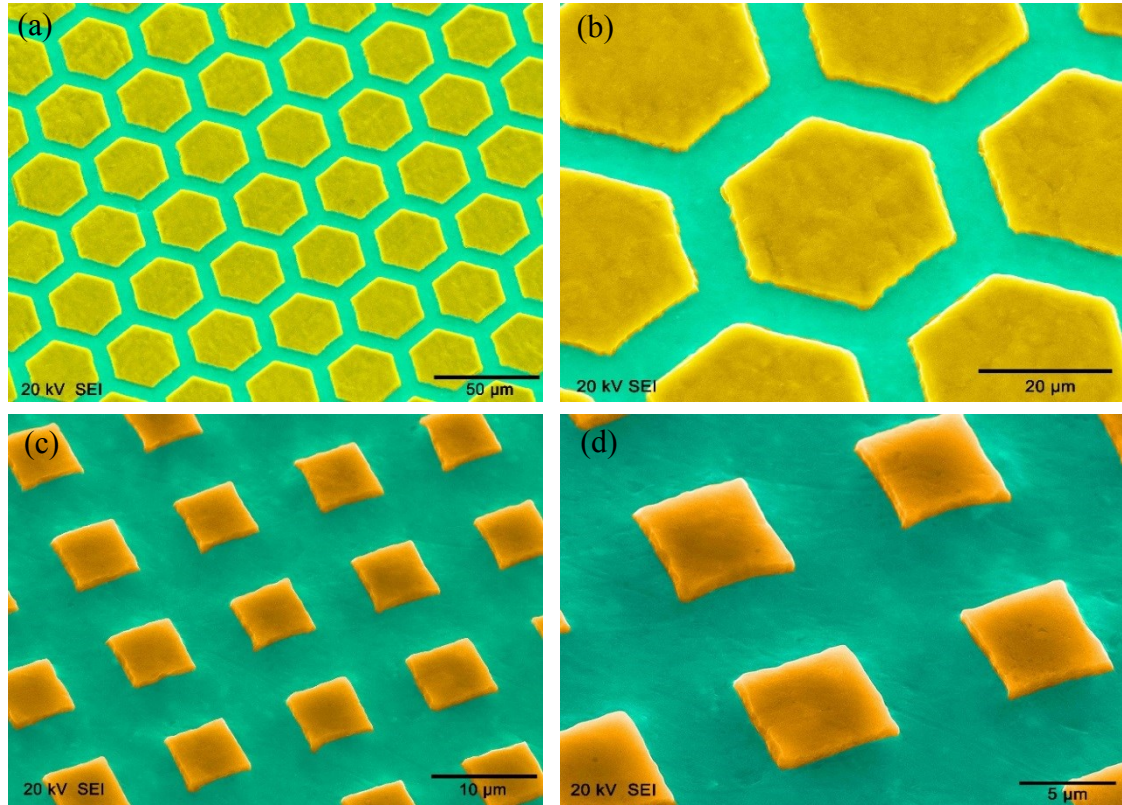


Figure 3.2.1. (a)-(b) Hexagonal and (c)-(d) square patterns created on aluminum with the laser fluence of  $6.2 \text{ J/cm}^2$ .

and due to the punch of the copper grid onto the sample. Figure 3.2.1(a) shows uniform patterns could be created over larger area of the sample. Figure 3.2.1(b) is a close up micrograph of the patterned region demonstrating that resulting pattern has very high fidelity. These topography images show that patterning of the pre-determined template is highly scalable where size and shape of the template allows precise control. Figures 3.2.1(c)-(d) show another patterning on the aluminum sample with fine square copper grids. The fine square grid has 2000 lines/inch, pitch width of  $12.5 \mu\text{m}$ , hole width  $7.5 \mu\text{m}$ , and bar width of  $5 \mu\text{m}$  with diameter of 3 mm. Figure 3.2.2 shows patterning on the gold thin foil with nickel square grids. Nickel square grid has 600 lines/inch, pitch width of  $42 \mu\text{m}$ , hole width  $30 \mu\text{m}$ , and bar width of  $16\text{-}10 \mu\text{m}$ , thickness of  $20 \pm 3 \mu\text{m}$  with the

diameter of 3 mm. It is evident that any geometry of the grids can be readily transferred onto several types of metallic alloys with very high precision. The laser beam can be scanned over the surface to produce the desired pattern at a larger scale. By changing the

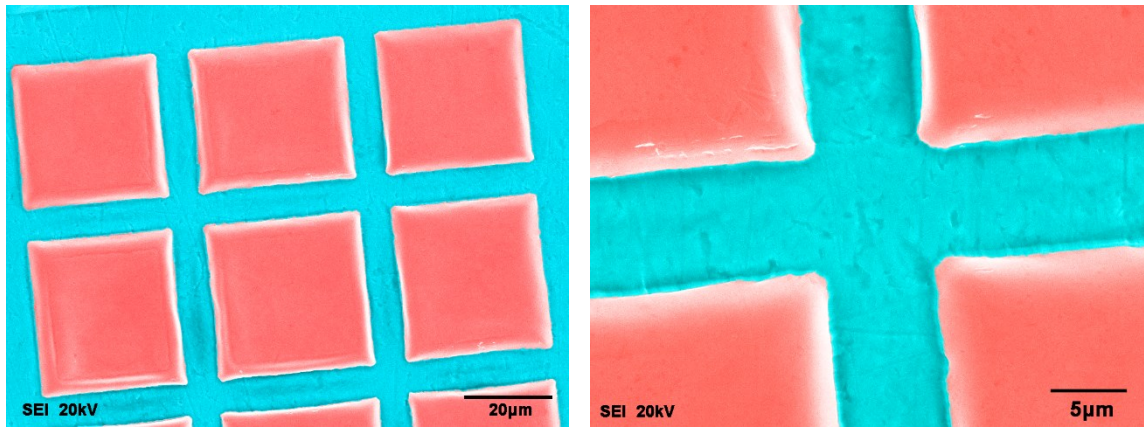


Figure 3.2.2. Square patterns on gold foil generated with the laser fluence of  $2.8 \text{ J/cm}^2$ .

number of pulses at each point and laser fluence, depth of the pattern can be controlled precisely.

ii. Laser-assisted imprinting of NiTi shape memory alloys

Figure 3.2.3 shows the patterning on the  $25 \text{ }\mu\text{m}$  thick NiTi foil with  $7.1 \text{ J/cm}^2$  laser fluence using the nickel mesh grid having the same dimensions as the one used in patterning the gold thin foil shown in Figure 3.2.2. It should be noted that the sample preparation of aluminum, gold, and the NiTi thin foil presented heretofore was performed by the ‘method M2’ where the mesh grid is placed in between the ablative layer and the sample to be patterned, demonstrated more in detail in Appendix A2. Figure 3.2.4 shows the patterning on the 1 mm thick NiTi sample when  $2 \text{ J/cm}^2$  is used. The square grid has 300 lines/inch, hole width  $58 \text{ }\mu\text{m}$ , pitch width of  $83 \text{ }\mu\text{m}$ , and bar width of  $25 \text{ }\mu\text{m}$  with diameter of 3 mm and thickness of  $20 \pm 3 \text{ }\mu\text{m}$ . However, this sample was prepared by the ‘method M1’ (details in Appendix A1) where initially a thin graphite ablative layer is

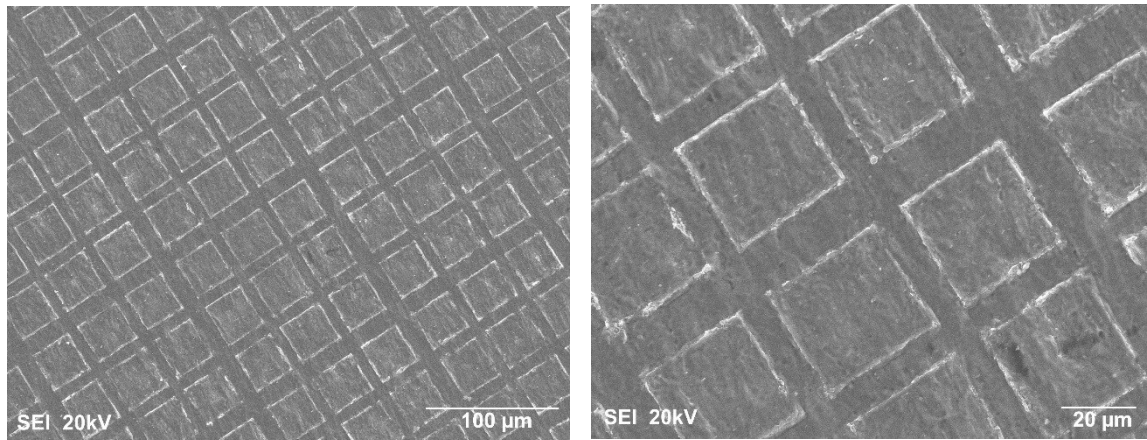


Figure 3.2.3. Square patterns on NiTi foil generated with the laser fluence of  $7.1 \text{ J/cm}^2$ . sprayed on the NiTi specimen and then the mesh grid is placed on it. These results indicate that patterns obtained on the samples prepared by the ‘method M2’ have relatively clean and undamaged surface microstructure, as well as the generated protrusions have sharp and well-defined edges, as evidenced from the SEM images shown above. One explanation to this could be that, since the laser-matter interaction and plasma formation primarily takes place on the ablative layer, aluminum thin foil in these cases, the sample to be patterned is kept from being directly exposed to laser beam, and thus avoid any possible damage that could result from the laser power. Consequently, the plasma formed on the aluminum ablative layer leads to the shock-wave generation that pushes the underlying mesh grid and creates such well-defined patterns. On the other hand, patterns generated on the samples prepared via the ‘method M1’, shown in Figure 3.2.4, reveal some melting and splashing of material along the protrusion edges. This could be due to the NiTi sample being indirectly exposed to the laser beam even though it is covered with a thin graphite ablative layer. All of the patterns were obtained with a single laser pulse, unless stated otherwise. Figure 3.2.5(a) shows the line scan of the patterned surface

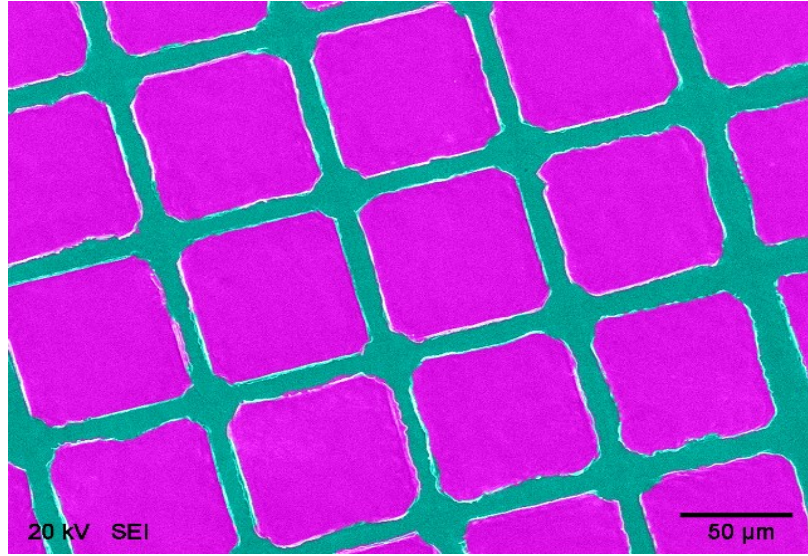


Figure 3.2.4. Square patterns generated on NiTi shape memory alloy with  $2 \text{ J/cm}^2$  laser fluence.

obtained with  $2 \text{ J/cm}^2$ . The average depth of the indent is around  $1.5 \text{ μm}$ . As expected, patterns that were generated on the surface have the similar dimensions as the copper grid.

In order to investigate and find the optimum laser parameters to achieve the highest and the smoothest patterns with high recovery ratio, patterns with different depths were obtained by changing laser energy between  $1.3\text{-}3.2 \text{ J/cm}^2$ . Figure 3.2.5(b) shows the change of the patterns' depth generated with respect to the laser fluence. These depth measurements are the average depth of 8 different points from 3 separate samples being irradiated by  $1.3\text{-}3.2 \text{ J/cm}^2$  laser power. The depth increases when the laser fluence increases. After around  $2.65 \text{ J/cm}^2$ , depth of the patterns is leveled off. Increasing the laser fluence increases the kinetic energy of the particles being ejected from the target. It is well known that above the ablation threshold, thickness or volume of material removed per pulse typically shows a logarithmic increase with fluence according to the Beer-Lambert law [86]. The trend in depth of the as-created patterns with respect to the laser fluence, in

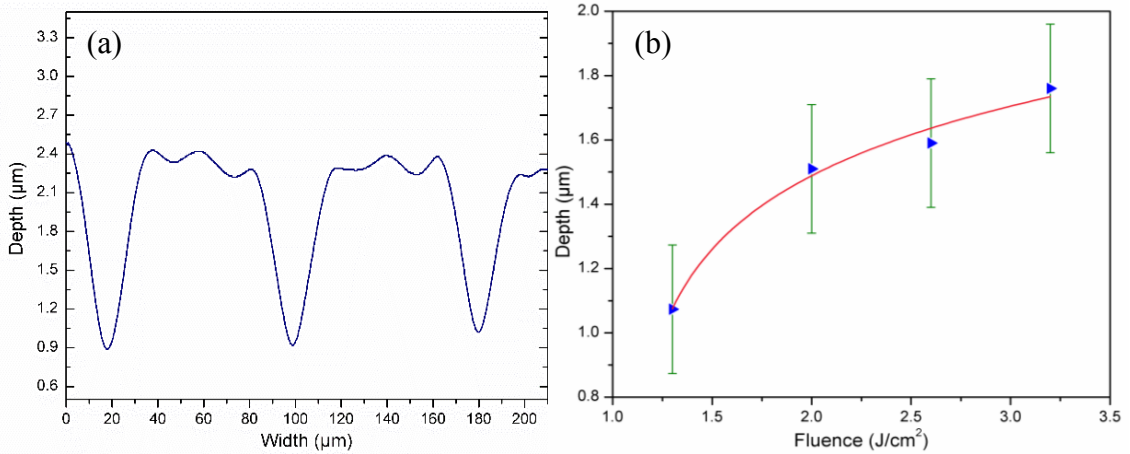


Figure 3.2.5. (a) 1D linear depth profile of square patterns obtained at  $2 \text{ J/cm}^2$  and (b) depth of patterns as a function of laser fluence on NiTi shape memory alloy

Figure 3.2.5(b), is a clear evidence of this law. The laser energy as a control parameter is known to significantly influence the morphology of patterns and to cause changes in the microstructure. Laser energy was shown to play an important role for surface patterning. Patterns generated on NiTi SMAs will allow to create controllable surface by temperature change (e.g. triggered by electrical current) which will activate SMAs and surface geometry will change upon phase transformation. Thus, transformed surfaces could generate very different drag or friction forces that can be optimized for aircraft operation. Further analysis is needed to find the optimum laser properties for recovery of the patterns and the influence of the shapes of the created patterns on friction and drag reduction.

### iii. Simulation of laser absorption on Copper surface

Since in the laser-assisted imprinting with preselected templates an ablative layer and a mesh grid is placed on NiTi, the laser primarily interacts with the mesh grid, and thus the shock wave generation mainly takes place on the template grids, such as the copper mesh grid. Hence, to better understand the pressure generation and its propagation,

a numerical simulation of pressure evolution in copper irradiated by a nanosecond pulsed laser (1064 nm wavelength, 10 Hz, 2 J/cm<sup>2</sup>, 3 mm beam diameter, 5 ns pulse width) were conducted using the fifth-order weighted essentially non-oscillatory finite volume method [92, 93] coupled with a Mie-Gruneisen model [94]. The energy flux due to the laser irradiation is modeled as a volumetric heat source in the energy equation. Beer's law with a Gaussian distribution describes the absorption of laser energy

$$Q(x, y, t) = I_0(1 - R)\alpha e^{\left(-\alpha(y_s - y) - \frac{(x - x_s)^2}{r_0^2} - \frac{t^2}{t_0^2}\right)}$$

where  $(x_s, y_s)$  is the surface coordinates of the laser beam center and  $z = y_s - y$  measures the depth from the surface. Here,  $I_0$ ,  $R$ ,  $\alpha$ ,  $t_0$  and  $r_0$  are laser energy intensity, reflectance, absorption coefficient, pulse width and the beam radius, respectively. In this study, the absorption coefficient is  $8.3 \times 10^7 \text{ m}^{-1}$  and the energy transferred by radiation is not considered. Figure 3.2.6 illustrates the surface pressure and temperature evolution

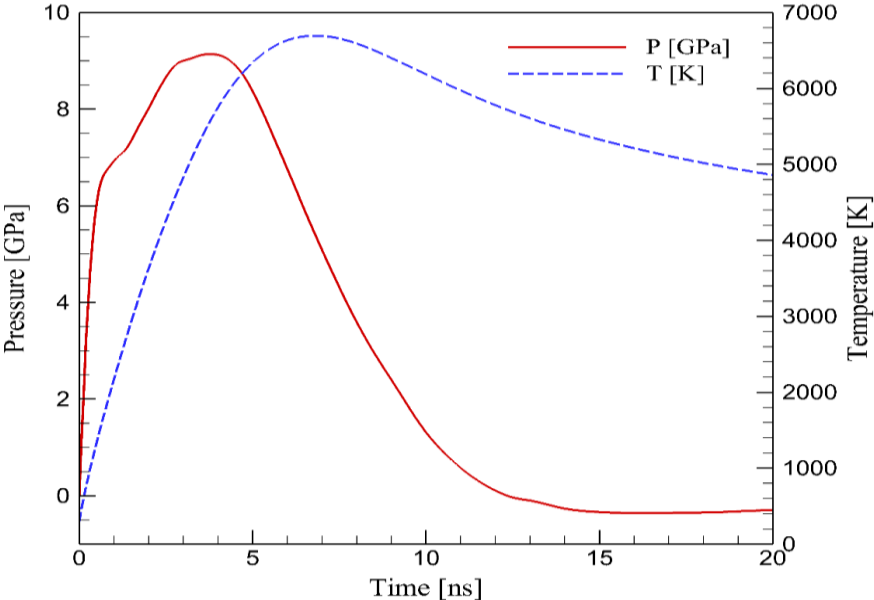


Figure 3.2.6. Pressure and temperature evolution on copper for the laser fluence of 2 J/cm<sup>2</sup>.

computed at  $(x_s, y_s)$  for  $2 \text{ J/cm}^2$ . Our simulation results show that pressure is strongly dependent on the value of total incident laser energy density and the peak pressure value increased with laser energy density. The hydrostatic pressure of  $> 8 \text{ GPa}$  and temperature of  $> 6000 \text{ K}$  could be generated when laser energy intensity of  $2 \text{ J/cm}^2$  laser pulse is used.

## CONCLUSION

Overall, two different, low cost, relatively fast, and highly scalable laser-assisted imprinting techniques for micro-patterning of metallic alloys, in particular NiTi shape memory alloys were reported. As a proof of concept, having patterned aluminum and gold with the hexagonal and fine square templates, it was also shown that almost any geometrical pattern with very high fidelity could be generated on a relatively wide array of alloys. Shape recovery of the as-generated patterns by the laser direct-scribing of the NiTi SMA was realized. The depth of the patterns for  $\text{Ni}_{50}\text{Ti}_{50}$  samples were shown to increase with laser energy density. The recovery measurement shows that more than 30% recovery could be obtained when a  $0.18 \text{ J/cm}^2$  laser fluence is used. Our results prove that indentation with laser shock-wave is an effective technique and a strong candidate to replace nanoindentation to obtain higher shape memory effect ratios. Laser energy was shown to play an important role for surface patterning. Controlling the thickness of the depth by varying the laser parameters is a unique feature of laser-assisted shock wave imprinting. In addition, no heating or etching is required in this technique. Unlike the most direct imprinting techniques which require high pressure which in turn results in damage to the sample, this technique can produce patterns without damaging the work-piece. It is relatively easy to have scalable product and expected to be a competitive technique for

advanced manufacturing. Also, numerical simulations were conducted to better understand the mechanism behind shock wave propagation and heat wave evolution on the surface as well as inside the material which agrees with experimental values.



## APPENDIX A: SAMPLE PREPARATION

### A1. Sample preparation of 'method M1'

This method utilizes thin graphite layer as an ablative layer.

1. Take the NiTi sample and place it over a paper towel as show in Figure A1.1.

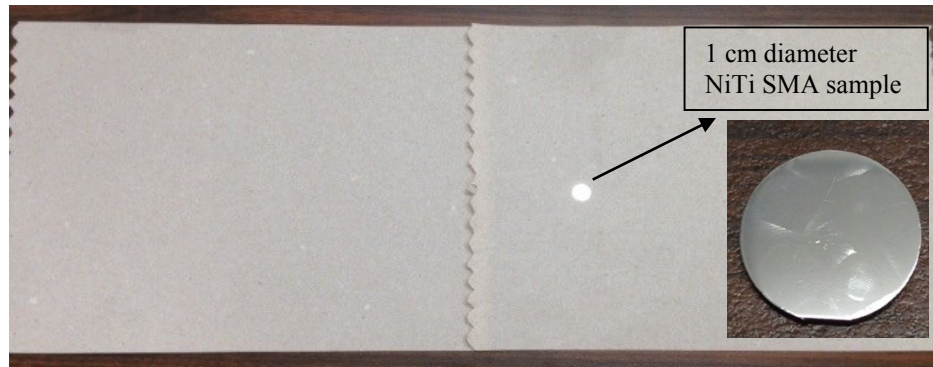


Figure A1.1

2. Next, take the Graphite spray (Blister) and shake it to make the solution uniform, then spray starting from left to right (in the direction of arrow shown below) for once. This results in approximately 10-15  $\mu\text{m}$  thick layer of graphite.

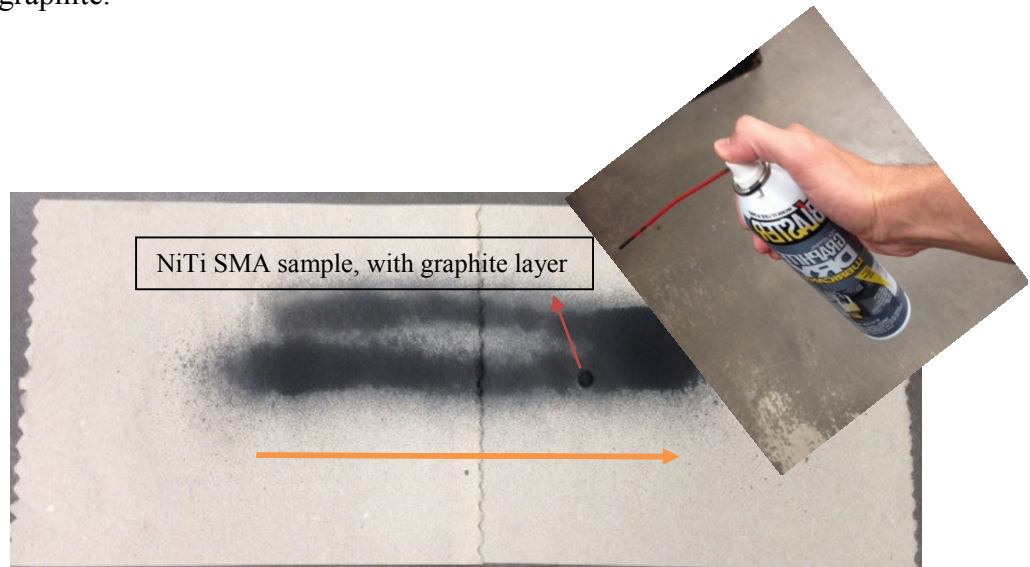


Figure A1.2

3. Place as many mesh grids the sample can accommodate like shown in Figure A1.2, in this case shown for three mesh grids on the graphite sprayed NiTi sample.



Figure A1.3

4. Cautiously take the sample (Figure A1.3) and place it over a piece of scotch-tape, shown in Figure A1.4.



Figure A1.4

5. Cut a transparent piece of glass (pre-cleaned micro slides from Sargent-Welch) in this case to approximately 2x2 cm square. Clean the surface of the cut glass using acetone and kimwipes (Kimtech). Place the piece onto another piece of scotch-tape, as in Figure A1.5. This glass will serve as the confinement medium.



Figure A1.5

6. Flip over the part prepared in step 5 and using a sharp blade (or similar cutting tool) cut and peel off the portion of the scotch-tape that will cover the part of the sample to be patterned, as shown in Figure A1.6. This is the part where the laser beam will be incident upon the sample.

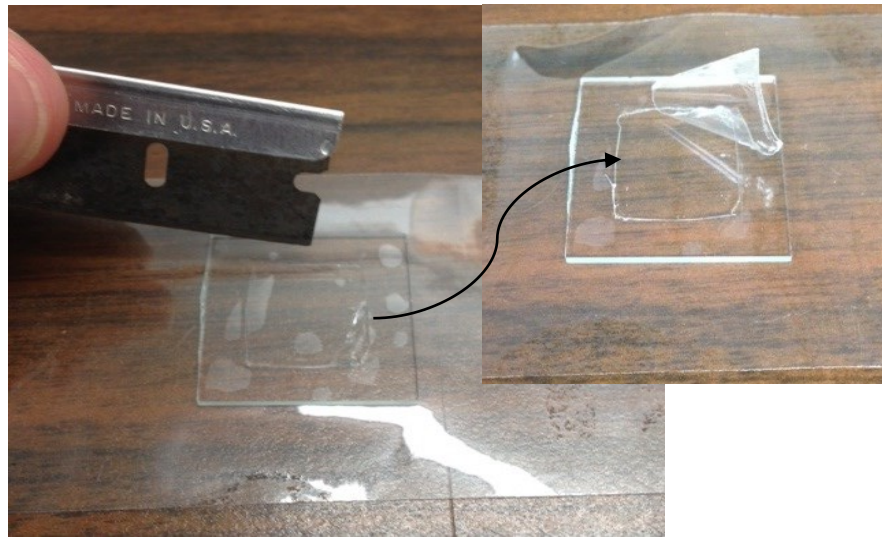


Figure A1.6

7. Next, take the piece prepared in step 6, the sticky part facing the sample, bring it slowly down to the piece prepared in step 4. Firmly stick both parts to each other as shown in Figure A1.7 making sure that the mesh grids are still in place. This is the final step of preparing the sample via ‘method M1’. The sample is ready to be taken to patterning.

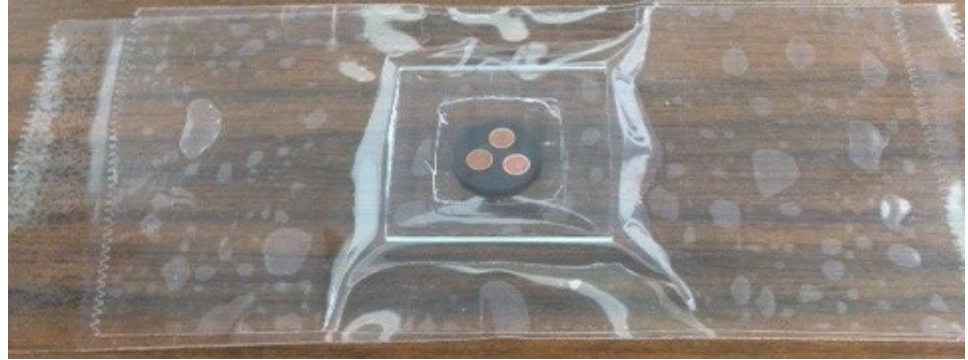


Figure A1.7

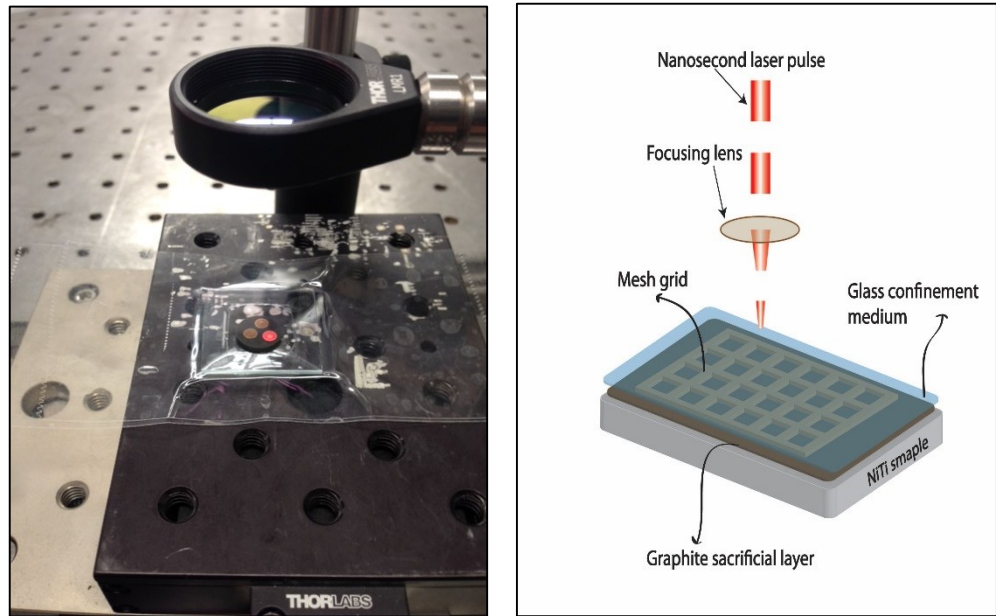


Figure A1.8. Sample preparation of ‘method M1’

## A2. Sample preparation of 'method M2'

This method utilizes thin aluminum foil (Reynolds) as an ablative layer. Preparation of both any thin foil samples and 1 mm thick NiTi samples is demonstrated simultaneously.

1. If the sample to be patterned is of thin foil form, cut it into smaller pieces as shown in Figure A2.1.

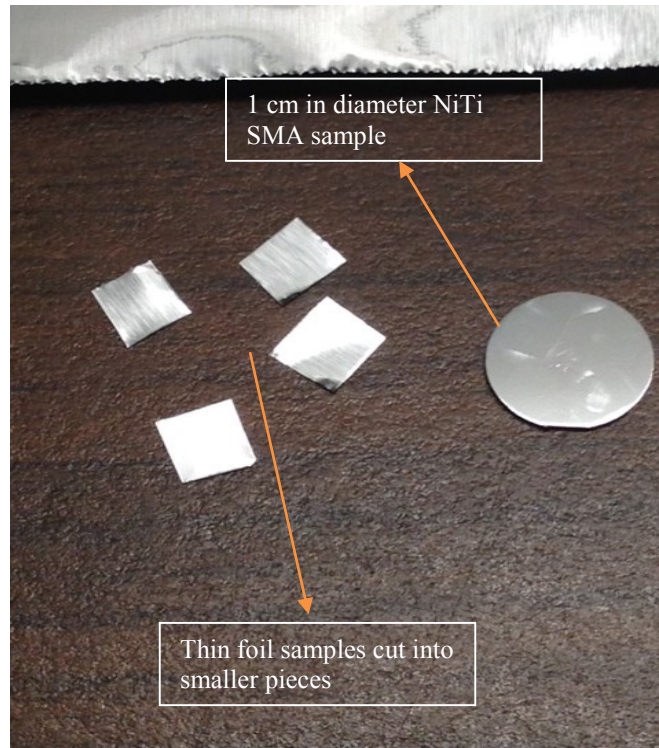


Figure A2.1

2. Next, place the smaller cut thin samples on a piece of glass (pre-cleaned micro slides from Sargent-Welch) in this case to approximately 2x2 cm square, this will serve as the base for the thin foil samples, in Figure A2.2. No need to place the 1 mm thick samples, since they are thick enough to stay undeformed during preparation.

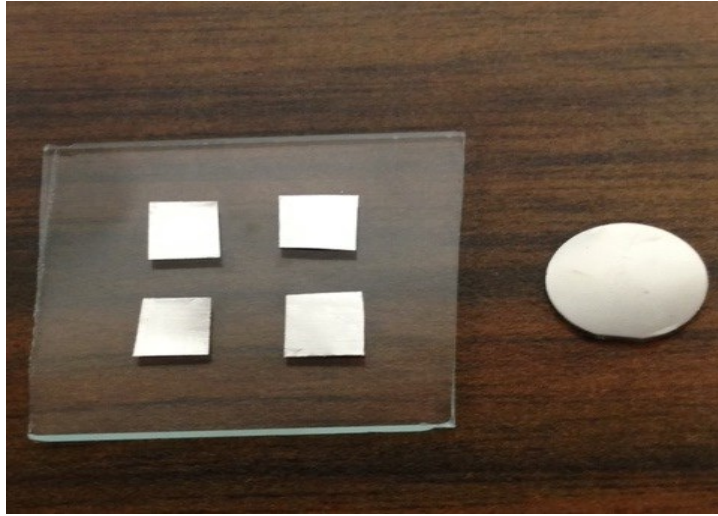


Figure A2.2

3. Place as many mesh grids the samples can accommodate like shown in Figure A2.3.



Figure A2.3

4. Next, take smaller cut thin aluminum foils (the same size as the smaller cut thin foil samples in step 1) and cautiously bring them onto the samples with mesh grids on, as in Figure 2.4. These pieces will serve as the ablative layer.

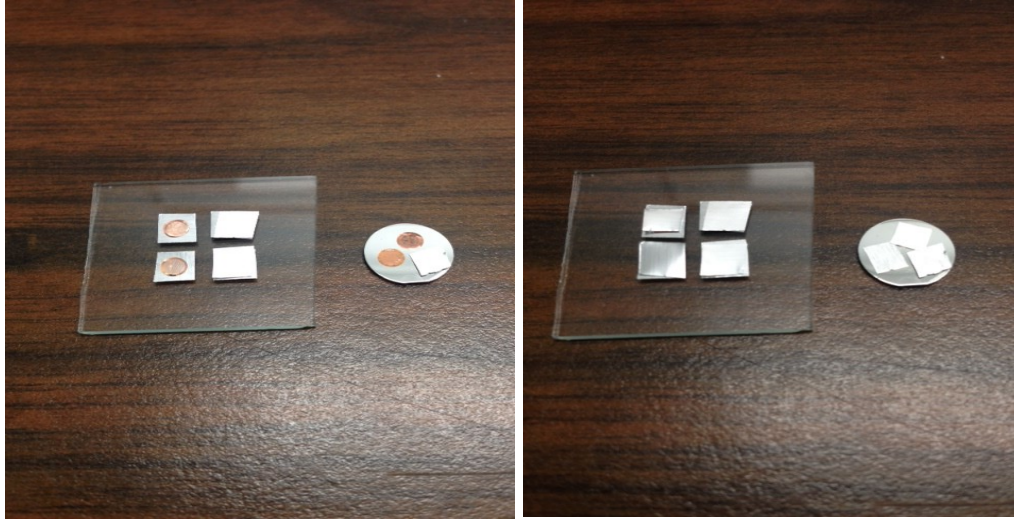


Figure A2.4

5. Place the pieces prepared in step 6 onto a piece of scotch-tape, as in Figure A4.5. This glass will serve as the confinement medium.



Figure A2.5

6. Cut a transparent piece of glass (pre-cleaned micro slides from Sargent-Welch) in this case to approximately 2x2 cm square. Clean the surface of the cut glass using acetone and kimwipes (Kimtech). Place the piece onto another piece of scotch-tape, as in Figure A2.6. This glass will serve as the confinement medium.



Figure A2.6

7. Flip over the part prepared in step 6 and using a sharp blade (or similar cutting instrument) cut and peel off the portion of the scotch-tape that will cover the part of the sample to be patterned, as shown in Figure A2.7. This is the part where the laser beam will be incident upon the sample.

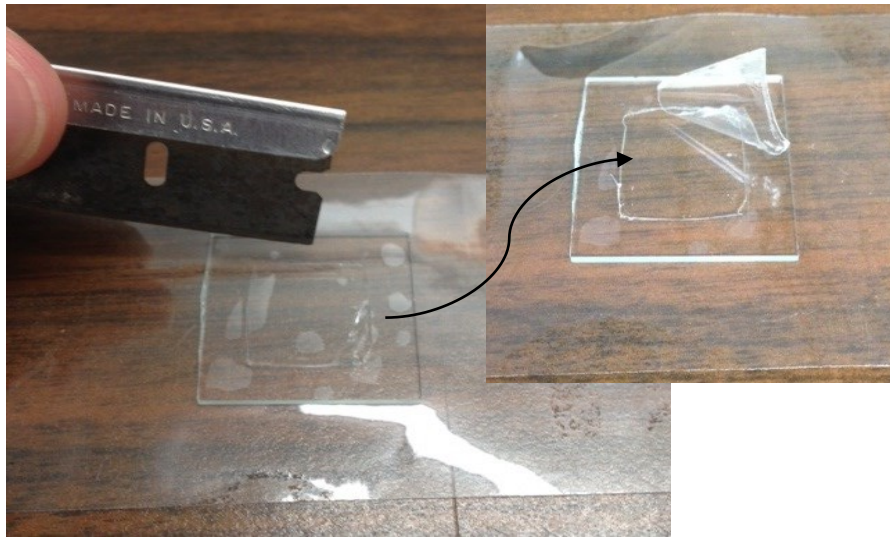


Figure A2.7

8. Before taking the pieces prepared in step 7, it is better to discharge them. What was observed during the preparation that the piece in step 7 statically charges up and once taken to put over the prepared samples (in step 5) the glass and the scotch tape pulls the thin aluminum ablative layer, mesh grids, and even the thin foil samples away from their places completely messing up with the samples. The way it is discharged is as follows: Aluminum foil is randomly cut into small pieces and the confinement layer glass piece (from step 7) is brought to close proximity of these pieces where it will attract the cut aluminum parts, as shown in Figure A2.8. Then the stuck pieces are removed



using a tweezers and this step is repeated until the confinement glass piece no longer attracts the aluminum cutouts.

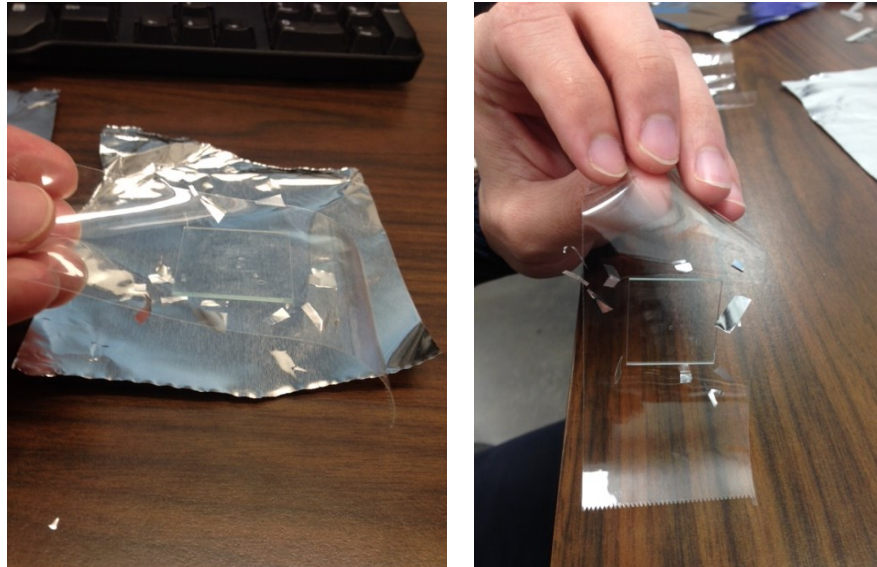


Figure A2.8

9. Next, take the pieces prepared in 8, the sticky part facing the sample, bring it slowly down to the pieces prepared in step 5. Firmly stick both parts to each other as shown in Figure A2.9 making sure that the ablative aluminum and mesh grids are still in place. This is the final step of preparing the sample via 'method M2'. The sample is ready to be taken to patterning.



Figure A2.9

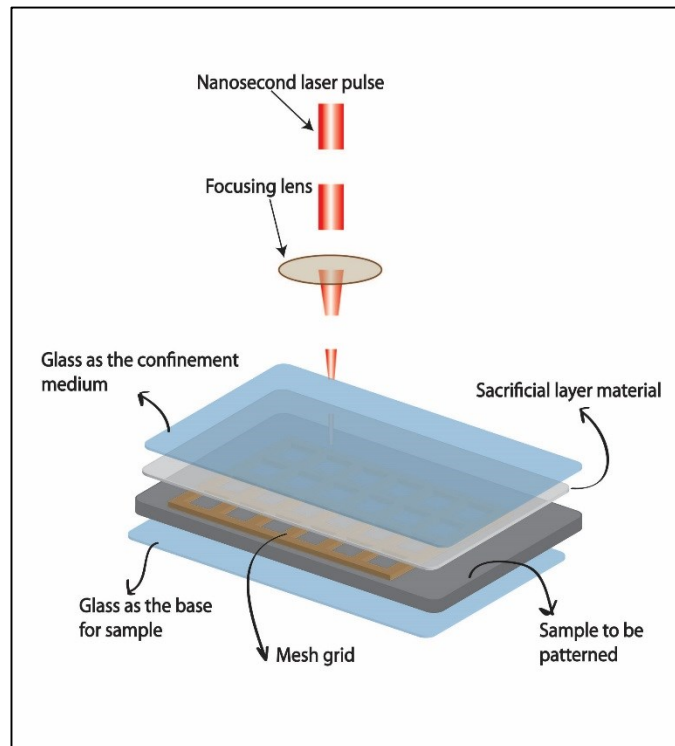
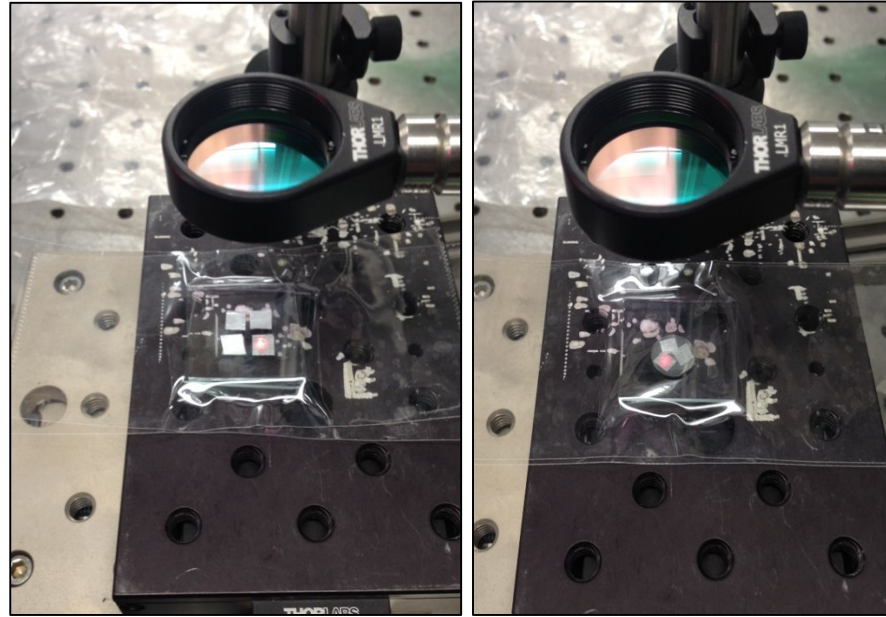


Figure A2.10. Sample preparation of 'method M2'

## APPENDIX B: Nd:YAG LASER OPERATION

Make sure that there is enough cooling water inside chiller located at the side of the laser main controller unit (big box on wheels). Once every month, water level must be checked.

### Turn ON Procedure:

1. Before turning ON the laser everyone in the lab must be wearing laser eye protection goggles.
2. Turn the laser ON by rotating the key-switch counter-clockwise until the key is horizontal (Figure B1). Immediately after the key switch is rotated to 'I' position, the LED screen will run through a three set of 3 digit numbers. These numbers “ $A_1A_2A_3$ ,  $B_1B_2B_3$ ,  $C_1C_2C_3$ ” in the order they appear on LED make up the number of shots the laser has been shooting since the last reset. The pump light tube of the laser must be changed after 30,000,000 shots.



Figure B1. Initial turn on procedure of a laser.

3. Allow about 10-15 seconds for the start of coolant system (water flow). Then the water flow will start.

4. All shutters must be in closed state. Shutter light on the laser controller must be off and the shutter on the front of the laser head must be closed.

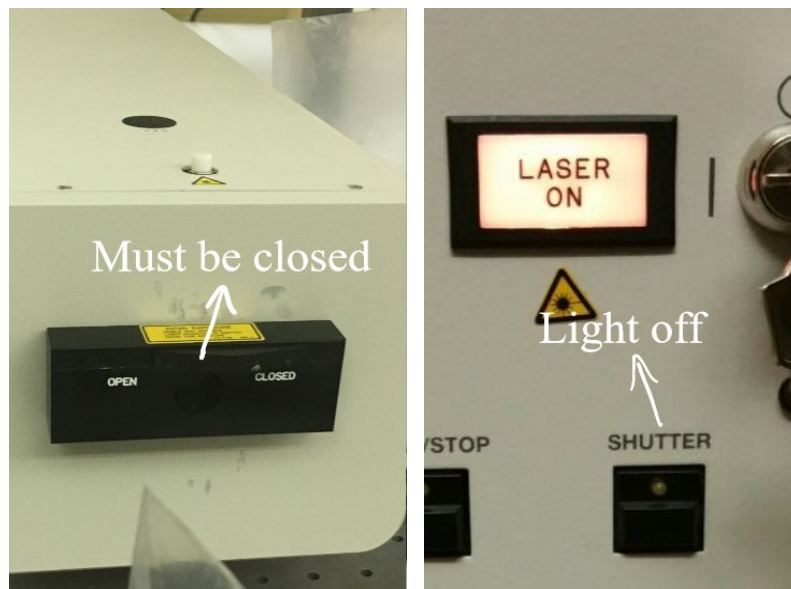


Figure B2. Shutter on the laser head (left) and the shutter button on laser controller (right).

5. Pressing the SELECT button on the laser controller multiple times lets one to toggle between different settings of the laser. One is the Q-switch and it is activated when the light led corresponding to it is lit. The Q-switch can be adjusted to a desired value using UP and DOWN buttons. Decreasing the Q-switch will increase the energy. However, changing the Q-Switch more than 10 units may change the beam properties (e.g. pulse duration, beam shape etc.). The value of Q-switch is set based on the experiment one does, for the most of the laser patterning experiments in this thesis it was set to 225.

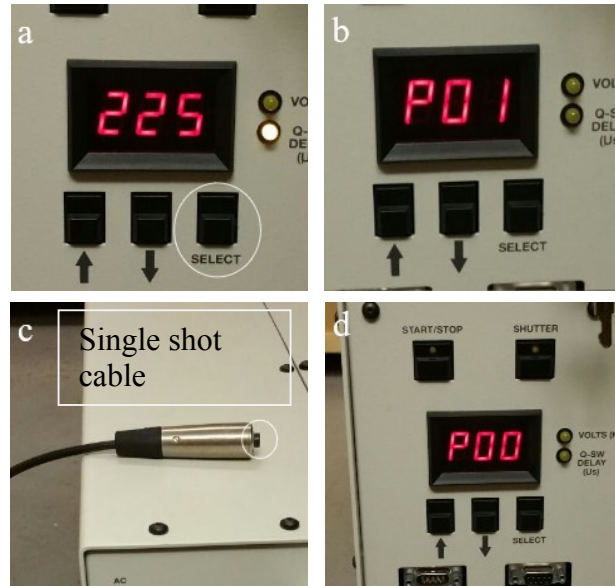


Figure B3. Summary of the procedure for single shot mode, a) press the SELECT button multiple times until b) P01 appears, c) press the single shot button once, d) P01 will change into P00.

6. By default the frequency of laser beam is 10 Hz. In this experiment, frequency does not need to be changed. However, if different value is needed, the SELECT button is pressed until the screen reads f10 and it is changed to the desired value using the UP and DOWN buttons

5. Next, the START button which is located near the shutter button on the laser controller should be pressed. The light will turn on and blink, laser will start and there will be continuous clicking sound.

6. Next, the following steps should be done to start the laser in either continuous pulse (P01) or single (manual) shot (P00) mode. Press the select button until the P01 reading appears on the screen of the laser controller (Figure B3). If this is the case, it means the laser is operating in continuous pulse mode.

7. To change the laser from the continuous pulse operation mode to manual single shot mode, the button on the single shot cable should be pressed once, it will change the P01 to P00 (Figure B3). The mode P00 is the single shot (manual) control mode. It is always safer to start the laser on P00 mode.

6. About 15 minutes should be allowed for the laser to warm up and stabilize.

7. STOP! Make sure that everyone wearing safety goggles.

8. Open the shutter at the front of the laser by sliding it to the left (Figure B4).



Figure B4. Opening the shutter on the front of the laser.

9. STOP! Follow the expected path of the laser beams to make sure it is safe and the laser does not hit the equipment in the lab (e.g. computer monitor, spectrometer etc.).

11. To adjust the energy of the laser use the halfwave plate and polarizer (Figure B5). Energy can be adjusted by rotating the halfwave plate. Rotation of halfwave plate in a

certain direction will decrease the energy for one of the beams while increasing the other one.

12. Beam will be split into two components by a polarizer in the direction of the initial beam and to the perpendicular to that direction. Block the unused beam from the one side of the polarizer with a beam dump (Figure B5).

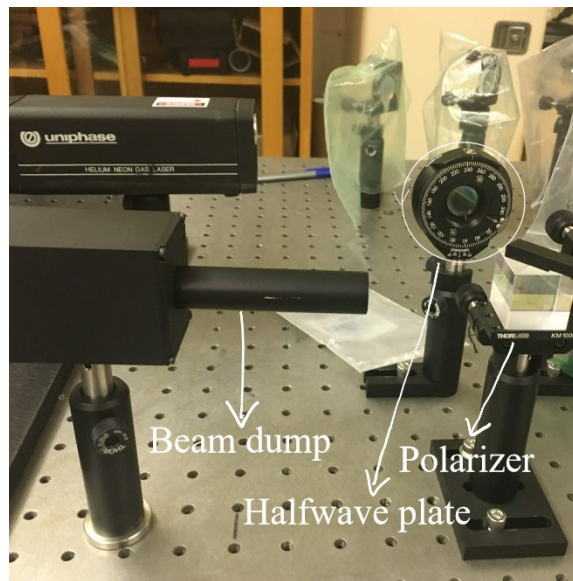


Figure B5.

13. Put the power meter to the other side of the polarizer that is going to be used. Adjust the height of the power meter so that the laser hits to the center.

14. After making sure that it is safe, open the shutter by pressing shutter button which is located on the controller of the laser (Figure B2). Light of the shutter button will be on.

15. Now the laser is on and it is controlled by a single shot button (P00 mode). Press the button once to release single laser beam, press and hold the button for 5 seconds to have continuous laser beams coming in a frequency that have been set before (P01 mode).

15. Adjust the energy of the laser to the desired value by rotating halfwave plate to either counter-clockwise or clockwise.

16. After adjusting the energy, press the single shot button to stop the laser (P00 mode).  
Align the laser to hit the target.

17. When the setup is ready and the laser is aligned properly, press and hold the single shot button to start the experiment.

#### Turn OFF Procedure:

1. Press the single shot button to stop the laser (P00 mode) (3cd).
2. Turn off the shutter by pressing the SHUTTER button on the laser controller. The shutter light should turn off.
3. Close the shutter on the front of the laser by sliding it to the right.
4. Press the SELECT button multiple times until the P00 screen appears.
5. Change P00 to P01 using UP button on the laser controller.
6. Press the START/STOP button to stop the laser. Continuous clicking sound should disappear.
7. Rotate the key switch clockwise to turn off the laser.
8. Cover the optics with plastic bags to prevent dust formation.



## Literature Cited:

1. Jani, J., Leary M, Subic A, Gibson MA (2014) A review of shape memory alloy research, applications and opportunities. *Materials & Design* 56:1078-113.
2. Humbeeck, J., (1999) Non-medical applications of shape memory alloys. *Mater. Sci. Eng. A*:134-48.
3. Sun, L., Huang WM, Ding Z, Zhao Y, Wang CC, Purnawali H, et al. (2012) Stimulus-responsive shape memory materials: a review. *Mater. Des.* 33:577-640.
4. Kohl, M., (2010) Shape memory microactuators (microtechnology and MEMS). 1 ed. Heidelberg: Springer-Verlag, Berlin.
5. Kahny, H., Huffz MA, Heuer AH (1998) The TiNi shape-memory alloy and its applications for MEMS. *Micromech. Microeng.* 8:213-21.
6. Fujita, H., Toshiyoshi H (1998) Micro actuators and their applications. *Microelectron J* 29:637-40.
7. Butera, F., Coda A, Vergani G (2007) Shape memory actuators for automotive applications. In: *Nanotec IT newsletter*. Roma: AIRI/nanotec IT:12-6.
8. Leo, D.J., Weddle C, Naganathan G, Buckley SJ (1998) Vehicular applications of smart material systems:106-16
9. Stoeckel, D., (1990) Shape memory actuators for automotive applications. *Mater. Des.* 11:302-7.
10. Bil, C., Massey K, Abdullah EJ (2013) Wing morphing control with shape memory alloy actuators. *J. Intell. Mater. Syst. Struct.* 24:879-98
11. Hartl, D.J., Lagoudas DC (2007) Aerospace applications of shape memory alloys. *Proc. Inst. Mech. Eng. Part G: J. Aerospace Eng.* 221:535-52.
12. McDonald, S.L., (1991) Shape memory alloy applications in space systems. *Mater. Des.*12:29-32.
13. Petrini, L., Migliavacca F (2011) Biomedical applications of shape memory alloys. *J. Metall* : 2011.
14. Song, C., (2010) History and current situation of shape memory alloys devices for minimally invasive surgery. *Open Med. Dev. J.* 2:24-31.
15. Morgan, N.B., (2004) Medical shape memory alloy applications-the market and its products. *Mater. Sci. Eng. A* 378:16-23
16. Machado, L.G., Savi MA (2003) Medical applications of shape memory alloys. *Braz. J. Med. Biol. Res.* 36:683-91.
17. Mantovani, D., (2000) Shape memory alloys: properties and biomedical applications. *JOM* 52:36-44
18. Duerig, T., Pelton A, Stöckel D (1999) An overview of nitinol medical applications. *Mater. Sci. Eng. A* 273-275:149-60.
19. Olander, A., (1932) An electrochemical investigation of solid cadmium-gold alloys. *AmChemSoc* 54(10):3819-33.
20. Buehler, W.J., Gilfrich JV, Wiley RC (1963) Effect of low-temperature phase changes on the mechanical properties of alloys near composition TiNi. *Appl Phys* 34(5):1475-7.
21. Cederström, J., Van Humbeeck J (1995) Relationship between shape memory material properties and applications. *J Phys IV France* 05 C2-335-C2-41.

22. Huang, W., (2002) On the selection of shape memory alloys for actuators. *Mater. Des.* 23:11-9.
23. Lagoudas, D.C., (2008) *Shape memory alloy: modeling and engineering applications*. Springer, New York.
24. Duering, T.W., Melton KN, Stöckel D, Wayman CM (eds) (1990) *Engineering aspects of shape memory alloys*. Butterworth-Heinemann, London.
25. Otsuka, K., Kakeshita T (2002) Science and technology of shape-memory alloys: new developments. *MRS Bulletin*, 27(2), 91-100.
26. Popov, P.A., (2005) *Constitutive modelling of shape memory alloys and upscaling of deformable porous media* (Doctoral dissertation, Texas A&M University).
27. Paranjape, H.M., (2014) *Modeling of shape memory alloys: phase transformation/plasticity interaction at the nano scale and the statistics of variation in pseudoelastic performance* (Doctoral dissertation, The Ohio State University).
28. Patoor, E., Lagoudas DC, Entchev PB, Brinson LC and Gao X (2006) Shape memory alloys, Part I: General properties and modeling of single crystals. *Mechanics of materials*, 38(5-6), 391-429.
29. Sugioka, K., Cheng Y (2014) Ultrafast lasers-reliable tools for advanced materials processing, *Light Sci. App.* 3, E149-12.
30. Fei, X., Grummon DS, Ye C, Cheng GJ and Cheng Y-T (2012) Surface form memory in niti shape memory alloys by laser shock indentation, *J. Mater. Sci.* 47, 2088-2094
31. Ozbay, E., (2006) Plasmonics: merging photonics and electronics at nanoscale dimensions, *Science* 311(5758), 189-193.
32. Shen, N., Ding H, Browers R, Yu Y, Pence CN, Ozbolat IT, Stanford CM (2015) Surface micropatterning of pure titanium for biomedical applications via high energy pulse laser peening, *Journal Of Micro And Nano-Manufacturing*, 3(1), 011005
33. Chou, S.Y., Krauss PR, Renstrom PJ (1995) Imprint of sub-25 nm vias and trenches in polymers. *Applied physics letters* 67(21), 3114-6.
34. Chou S.Y, K.P., Renstrom PJ (1996) Imprint lithography with 25-nanometer resolution. *Science*, 272(5258), 85-7.
35. Guo, L.J., (2007) Nanoimprint lithography: methods and material requirements. *Advanced materials*, 19(4), 495-513.
36. Colburn, M., Grot A, Choi BJ, Amistoso M, Bailey T, Sreenivasan SV, Ekerdt JG, Grant Willson C (2001) Patterning nonflat substrates with a low pressure, room temperature, imprint lithography process. *Journal of Vacuum Science & Technology B: Microelectronics and Nanometer Structures Processing, Measurement, and Phenomena*, 19(6), 2162-72.
37. Bailey, T., Choi BJ, Colburn M, Meissl M, Shaya S, Ekerdt JG, Sreenivasan SV, Willson CG (2000) Step and flash imprint lithography: Template surface treatment and defect analysis. *Journal of Vacuum Science & Technology B: Microelectronics and Nanometer Structures Processing, Measurement, and Phenomena*, 18(6), 3572-7.
38. Leo, D.J., (2007) *Engineering Analysis of Smart Material Systems*, John Wiley & Sons, New Jersey.

39. Ye, C., Cheng GJ (2012) Scalable patterning on shape memory alloy by laser shock assisted direct imprinting. *Applied Surface Science*, 258(24), 10042-6.
40. Gao, H., Hu Y, Xuan Y, Li J, Yang Y, Martinez RV, Li C, Luo J, Qi M, Cheng GJ (2014) Large-scale nanoshaping of ultrasMOOTH 3D crystalline metallic structures. *Science*, 346(6215), 1352-6.
41. Bardy, S., Aubert B, Berthe L, Combis P, Hébert D, Lescoute E, Rullier JL, Videau L (2016) Numerical study of laser ablation on aluminum for shock-wave applications: development of a suitable model by comparison with recent experiments. *Optical Engineering*, 56(1), 011014.
42. Wang, Z., Feng G, Han J, Wang S, Hu R, Li G, Dai S, Zhou S (2016) Fabrication of microhole arrays on coated silica sheet using femtosecond laser. *Optical Engineering*, 55(10), 105101.
43. Fabbro, R., Fournier J, Ballard P, Devaux D, Virmont J (1990) Physical study of laser-produced plasma in confined geometry. *Journal of Applied Physics*. 68(2):775-784.
44. Anderholm, N.C., (1968) Laser generated pressure waves. *Bull. Am. Phys. Soc.* 13:388.
45. Anderholm, N.C., (1970) Laser generated stress waves. *Appl. Phys. Lett.* 16(3):113-115.
46. Fairand, B., Wilcox BA, Gallagher WJ, Williams DN (1972) Laser shock-induced microstructural and mechanical property changes in 7075 aluminum. *Journal of Applied Physics* 43(9):3893-5.
47. Clauer, A.H., Holbrook JH, Fairand BP (1981) Effects of laser induced shock waves on metals. In *Shock Waves and High-Strain-Rate Phenomena in Metals*: 675-702. Springer US.
48. Richard, T.D., (1971) Laser scribing apparatus. US Patent 3626141.
49. El-Kady, M.F., Strong V, Dubin S, Kaner RB (2012) Laser scribing of high-performance and flexible graphene-based electrochemical capacitors. *Science*. 335(6074):1326-30.
50. Wagner, R.E., (1974) Laser drilling mechanics. *Journal of Applied Physics* 45(10):4631-7.
51. Hackel, L., Rankin J, Racanellia T, Mills T, Campbell JH (2015) Laser peening to improve fatigue strength and lifetime of critical components. *Procedia Eng.* 133:545-555.
52. Gujba, A.K., Medraj M (2014) Laser peening process and its impact on materials properties in comparison with shot peening and ultrasonic impact peening. *Materials* 7:7925-7974.
53. Nie, X.F., He WF, Li QP, Long ND, Chai Y (2013) Experiment investigation on microstructure and mechanical properties of TC17 titanium alloy treated by laser shock peening with different laser fluence. *J. Laser Appl.* 25:1892-1898.
54. Ge, M.Z., Xiang JY (2016) Effect of laser shock peening on microstructure and fatigue crack growth rate of AZ31B magnesium alloy. *J. Alloys Compd.* 680:544-552.
55. Carpio, F.J., Araujo D, Pacheco FJ (2003) Fatigue behavior of laser machined 2024-T3 aeronautic aluminum alloy. *Appl. Surf. Sci.* 208-209:194-198

56. Dorman, M., Toparli MB, Smyth N, Cini A, Fitzpatrick ME, Irving PE (2012) Effect of laser shock peening on residual stress and fatigue life of clad 2024 aluminum sheet containing scribe defects. *Mater. Sci. Eng. A* 548:142-151.
57. Er, Ali. O., Chen J, Tang J, Rentzepis PM (2012) Coherent acoustic wave oscillations and melting on Ag(111) surface by time resolved x-ray diffraction. *Appl. Phys. Lett.* 100:51910-5.
58. Chrisey, D.B., Hubler GK (1994) *Pulsed Laser Deposition of Thin Films*: Wiley.
59. Sun, Z., Huang SM, Lu YF, Chen JS, Li YJ, Tay BK, Lau SP, Chen GY, Sun Y (2001) Field emission from polymer-converted carbon films by ultraviolet radiation. *Applied Physics Letters*, 78(14), 2009-11.
60. Huang, S.M., Lu YF, Sun Z (1999) Conversion of diamond clusters from a polymer by Nd: YAG pulsed laser (532 nm) irradiation. *Applied surface science*, 151(3-4), 244-50.
61. Gamaly, E.G., Rode AV, Luther-Davies B (1999) Ultrafast ablation with high-pulse-rate lasers. Part I: Theoretical considerations. *Journal of Applied Physics*, 85(8), 4213-21.
62. Pronko, P.P., Dutta SK, Du D, Singh RK (1995) Thermophysical effects in laser processing of materials with picosecond and femtosecond pulses. *Journal of Applied Physics*, (10), 6233-40.
63. Elsayed-Ali H.E., N.T., Pessot MA, Mourou GA (1987) Time-resolved observation of electron-phonon relaxation in copper. *Physical Review Letters*, 58(12), 1212.
64. Qian, M., Zhou YS, Gao Y, Park JB, Feng T, Huang SM, Sun Z, Jiang L, Lu YF (2011) Formation of graphene sheets through laser exfoliation of highly ordered pyrolytic graphite. *Applied Physics Letters* 98(17), 173108.
65. Berthe, L., Fabbro R, Peyre P, Bartnicki E (1999) Wavelength dependent of laser shock-wave generation in the water-confinement regime. *Journal of Applied Physics*, 85(11), 7552-5.
66. Amoroso, S., Bruzzese R, Spinelli N, Velotta R (1999) Characterization of laser-ablation plasmas. *Journal of Physics B: Atomic, Molecular and Optical Physics*, 32(14), R131.
67. Eason, R., (2007) *Pulsed Laser Deposition of Thin Films Applications-Led Growth of Functional Materials*: Wiley.
68. Peyre, P., Berthe L, Scherpereel X, Fabbro R, Bartnicki E (1998) Experimental study of laser-driven shock waves in stainless steels. *J. Appl. Phys.* 84:5985-5992.
69. Millett, J.C.F., Bourne NK, Gray GT, Stevens GS (2002) On the shock response of the shape memory alloy, NiTi. *AIP Conference Proceedings* 620:579-582.
70. Ni, W., Cheng YT, Grummon DS (2003) Microscopic superelastic behavior of a nickel-titanium alloy under complex loading conditions. *Applied Physics Letters* 82(17):2811.
71. Ma, X., Komvopoulos K (2003) Nanoscale pseudoelastic behavior of indented titanium-nickel films. *Applied Physics Letters* 83(18):3773-3775.
72. Zhang, Y.J., Cheng YT, Grummon DS (2005) Indentation stress dependence of the temperature range of microscopic superelastic behavior of nickel-titanium thin films. *Journal of Applied Physics* 98(3):033505.

73. Li, P., Karaca HE, Cheng YT (2015) Spherical indentation of NiTi-based shape memory alloys. *Journal of Alloys and Compounds* 651:724-730.
74. Ni, W., Cheng YT, Grummon DS (2002) Recovery of microindents in a nickel-titanium shape-memory alloy: a “self-healing” effect”. *Applied Physics Letters* 80(18):3310-3312.
75. Birnbaum, A.J., Yao YL (2010) The effects of laser forming on NiTi superelastic shape memory alloys. *Journal of Manufacturing Science and Engineering* 132(4):041002.
76. Zhang, Y., Cheng YT, Grummon DS (2006) Two-way indent depth recovery in a NiTi shape memory alloy. *Applied Physics Letters* 88(13):131904.
77. Thill, C.L., Etches J, Bond I, Potter K, Weaver P (2008) Morphing skins. *The aeronautical journal*, 112(1129), 117-39.
78. Jiménez, J., (2004) Turbulent flows over rough walls. *Annu. Rev. Fluid Mech.*, 36:173-96.
79. Bechert, D.W., Bruse M, Hage W (2000) Experiments with three-dimensional riblets as an idealized model of shark skin. *Experiments in fluids*, 28(5), 403-12.
80. Klocke, F., Feldhaus B, Mader S (2007) Development of an incremental rolling process for the production of defined riblet surface structures. *Production Engineering*, 1(3), 233-7.
81. Cheng, Y.T., Grummon DS (2008) Indentation in shape memory alloys. In *Micro and Nano Mechanical Testing of Materials and Devices*, pp. 69-84, Springer, Boston, MA.
82. Zhang, Y., Cheng YT, Grummon DS (2006) Shape memory surfaces. *Applied physics letters*, 89(4), 041912.
83. Ilhom, S., Seyitliyev D, Kholikov K, Thomas Z, Ali OE, Li P, Karaca HE, San O (2018) Laser shock wave-assisted patterning on NiTi shape memory alloy surfaces. *Shape Memory and Superelasticity*. 4(1), 224-31.
84. Ilhom, S., Kholikov K, Li P, Ottman C, Sanford D, Thomas Z, San O, Karaca HE, Ali OE (2018) Scalable patterning using laser-induced shock waves. *Optical Engineering* 57(4), 041413.
85. Bäuerle, D.W., (2011) *Laser processing and chemistry*. Springer-Verlag, Berlin.
86. Brown, M.S., Craig BA (2010) Fundamentals of laser-material interaction and application to multiscale surface modification. *Laser Precision Microfabrication* 135: 91-120.
87. Tamhankar, A., Patel R (2011) Optimization of UV laser scribing process for light emitting diode sapphire wafers. *Journal of Laser Applications* 23(3):032001.
88. Forsman, A.C., Banks PS, Perry MD, Campbell EM, Dodell AL, M. S. Armas MS (2005) Double-pulse machining as a technique for the enhancement of material removal rates in laser machining of metals. *Journal of Applied Physics* 98(3):033302.
89. Kaya, I., Tobe H, Karaca HE, Acar E, Chumlyakov Y (2016) Shape memory behavior of [111]-oriented NiTi single crystals after stress- assisted aging. *Acta Metallurgica Sinica (English Letters)* 29(3):282-286
90. Kaya, I., Tobe H, Karaca HE, Nagasako M, Chumlyakov Y (2015) Positive and negative two-way shape memory effect in [111]-oriented Ni<sub>51</sub>Ti<sub>49</sub> single crystals. *Materials Science and Engineering A* 639:42-53.

91. Atli, K.C., Karaman I, Noebe RD, Bigelow G, Gaydos D (2015) Work production using the two-way shape memory effect in NiTi and a Ni-rich NiTiHf high-temperature shape memory alloy. *Smart Materials and Structures* 24(12):125023.
92. Titarev, V.A., Romenski EF, Toro EF (2008) MUSTA-type upwind fluxes for non-linear elasticity. *Int. J. Numer. Meth. Engrn.* 73: 897-926.
93. San, O., Kara K (2015) Evaluation of Riemann flux solver for WENO reconstruction schemes: Kelvin-Helmholtz instability, *Comput. Fluids* 117: 24-41.
94. Mehmandoust, B., Pischevar AR (2009) An eulerian particle level set method for compressible deforming solids with arbitrary EOS. *Int. J. Num. Meth. Eng.* 79(10):1175-1202.
95. Hoashi, E., Yokomine T, Shimizu A, Kunugi T, Numerical analysis of wave-type heat transfer propagating in a thin foil irradiated by short-pulsed laser. *Int. J. Heat Mass. Trans.* 46(21):4083-4095.
96. Johnson, P.B., Christy RW (1974) Optical constants of transition metals: Ti, V, Cr, Mn, Fe, Co, Ni, and Pd. *Phys. Rev. B.* 9:5056-5070.